Linking Atmospheric Transport Resistance to Extreme Snowfall Risk Using Non-Stationary Extreme Value Models

Hiroshi MATSUDA[1*] and Shin'ichi HOMMA[1]

[1] Kokusai Kogyou Co., Ltd.,
2-24-1, Harumi-cho, Fuchu-shi, Tokyo 183-0057

[*]Corresponding author: hiroshi_matsuda@kk-grp.jp

Abstract

This study develops a hybrid physical–statistical framework for evaluating extreme snowfall risk along the Sea of Japan coast by integrating causal-network analysis, Dijkstra-based atmospheric transport physics, and non-stationary extreme value theory. Using a 135-year record (1889–2024) of annual maximum snow-depth anomalies from 23 meteorological stations, we first quantify atmospheric moisture transport pathways through a meteorological transport-cost model based on Dijkstra's shortest-path algorithm, incorporating distance, topographic barriers, and wind-direction penalties. The transport-cost analysis supports a physically consistent four-block spatial classification (Hokkaido, Tohoku, Hokuriku/Niigata, and San-in/Kinki) and identifies Hokuriku/Niigata as a low-resistance transport hub. Non-stationary Generalized Extreme Value (GEV) models driven by a local winter monsoon index (MOI_{SN}) reveal strong regional contrasts in monsoon sensitivity. The Hokuriku/Niigata block exhibits the highest sensitivity ($\beta_2 = 12.067$), while station-specific Bayesian analyses identify localized hotspots at Shirakawa ($\beta_2 = 26.238$), Takada ($\beta_2 = 22.722$), and Nagaoka ($\beta_2 = 18.116$). A direct comparison between transport cost (c_a) and monsoon sensitivity (β_2) demonstrates a strong negative relationship at both the regional-block scale ($r = -0.95$) and the station scale ($r = -0.52$, $p = 0.011$), indicating that reduced atmospheric transport resistance is systematically associated with increased extreme-snowfall sensitivity. Although long-term climatological trends generally indicate declining snowfall baselines ($\beta_1 < 0$), positive shape parameters in Hokuriku/Niigata ($\xi = 0.166$) reveal heavy-tailed Fréchet behavior and elevated susceptibility to rare high-impact events. These results demonstrate a decoupling between mean climatic trends and extreme-event risks: average snowfall may decline under warming conditions, while extreme snowfall hazards remain strongly amplified when intense winter monsoon surges propagate through low-resistance transport pathways. The proposed framework provides a physically interpretable approach for linking atmospheric transport processes with non-stationary extreme climate risks.

Keywords: Extreme snowfall; Non-stationary GEV; Dijkstra shortest path; Meteorological transport cost; Winter monsoon; Climate risk; Sea of Japan

1 Introduction

The Sea of Japan side of the Japanese archipelago is recognized as one of the heaviest seasonal snowfall regions globally. This extreme snowfall is primarily driven by the interaction between the cold Siberian air masses of the East Asian winter monsoon (EAWM) and the warm Tsushima Current flowing through the Sea of Japan. The subsequent forced orographic lifting by the central backbone mountain ranges of Japan, coupled with the meso-scale organization of convective snow clouds such as the Japan-Sea Polar-airmass Convergence Zone (JPCZ), triggers highly localized extreme snowfall events [5]. Given the profound societal, economic, and civil engineering impacts of these extreme weather events, understanding their long-term spatiotemporal variations is of critical importance for regional disaster mitigation and climate change adaptation.

Historically, numerous climatological studies have investigated the long-term variations of snowfall and maximum snow depth along the Sea of Japan. Standard observational analyses have reported gradual, centennial-scale decreasing trends in annual maximum snow depths, particularly in lower-latitude, southwest regions of Japan where the local air temperature is close to the rain-snow transition boundary [19]. However, traditional analytical approaches often rely on simple linear regressions or isotropic correlation networks, which fail to distinguish direct causal dependencies from spurious correlations induced by macroscopic common factors (such as synoptic-scale atmospheric circulations). While recent data-driven causal network discovery techniques, such as the Graphical Lasso and Linear Non-Gaussian Acyclic Models (LiNGAM), have emerged as powerful tools to map spatial dependencies [15, 16], purely statistical, causally inferred networks are frequently criticized as "black-box" formulations that lack physical and meteorological validation. Furthermore, statistical network searches can yield high directional volatility and leave extensive, topographically complex mountain zones, such as the Tohoku region, unclassified as statistical "blank areas" due to high localized volatility.

To resolve these physical and statistical limitations, this study proposes a novel, transferable hybrid framework that bridges purely data-driven spatiotemporal causal networks with physics-based transport models. As conceptually illustrated in the Two-Stage Hybrid Pipeline in Figure 1, our approach reconciles statistical causality with meteorological physics. In Stage 1 (Statistical Network Discovery), we utilize Graphical Lasso to systematically filter out macroscopic confounding noise and construct a sparse partial correlation network, which is subsequently fed into the DirectLiNGAM algorithm to estimate the directional causal dependencies and recursive orderings among localized stations. In Stage 2 (Physical Validation and Risk Assessment), we formulate a Dijkstra-based meteorological transport cost model, where transport resistance is parameterized by winds, distances, and orographic lifting penalties. This physical cost structure is used to provide physical support for the causally-discovered blocks and resolve statistical ambiguities by explicitly defining Tohoku as a topographic transition zone. Finally, we parameterize a non-stationary Generalized Extreme Value (GEV) distribution using a custom local winter monsoon intensity index (MOI_{SN}) to evaluate time-varying extreme risks. This hybrid pipeline operates under the paradigm of physics-informed data analysis, ensuring that purely data-driven network boundaries are grounded in physically interpretable transport resistance constraints.

The primary methodological and conceptual contribution of this work is two-fold. First, to our knowledge, no previous study has jointly integrated causal network discovery, physical transport modeling, and state-space trend extraction within a unified analysis pipeline. This hybrid integration significantly enhances model explainability and strengthens the robust execution of non-stationary extreme value analysis in topographically complex environments. Second, as a representative case study, we apply this unified framework to a unique 135-year historical instrumental record (1889–2024) of annual maximum snow depth anomalies across 23 representative meteorological stations in Japan. This century-scale empirical analysis reveals a physically interpretable decoupling between the gradual decline of the climatological snowfall baseline and the sustained sensitivity of extreme snowfall risk to intense winter monsoon events (referred to as the "Risk Jump," which represents a transient, sharp upward shift in extreme snowfall risk driven by intense monsoon surges).

The remainder of this paper is structured as follows. Section 2.2 describes the mathematical formulations of the Dijkstra meteorological transport cost, the spatial causal network algorithms, the local winter monsoon index, and the state-space and non-stationary GEV models.

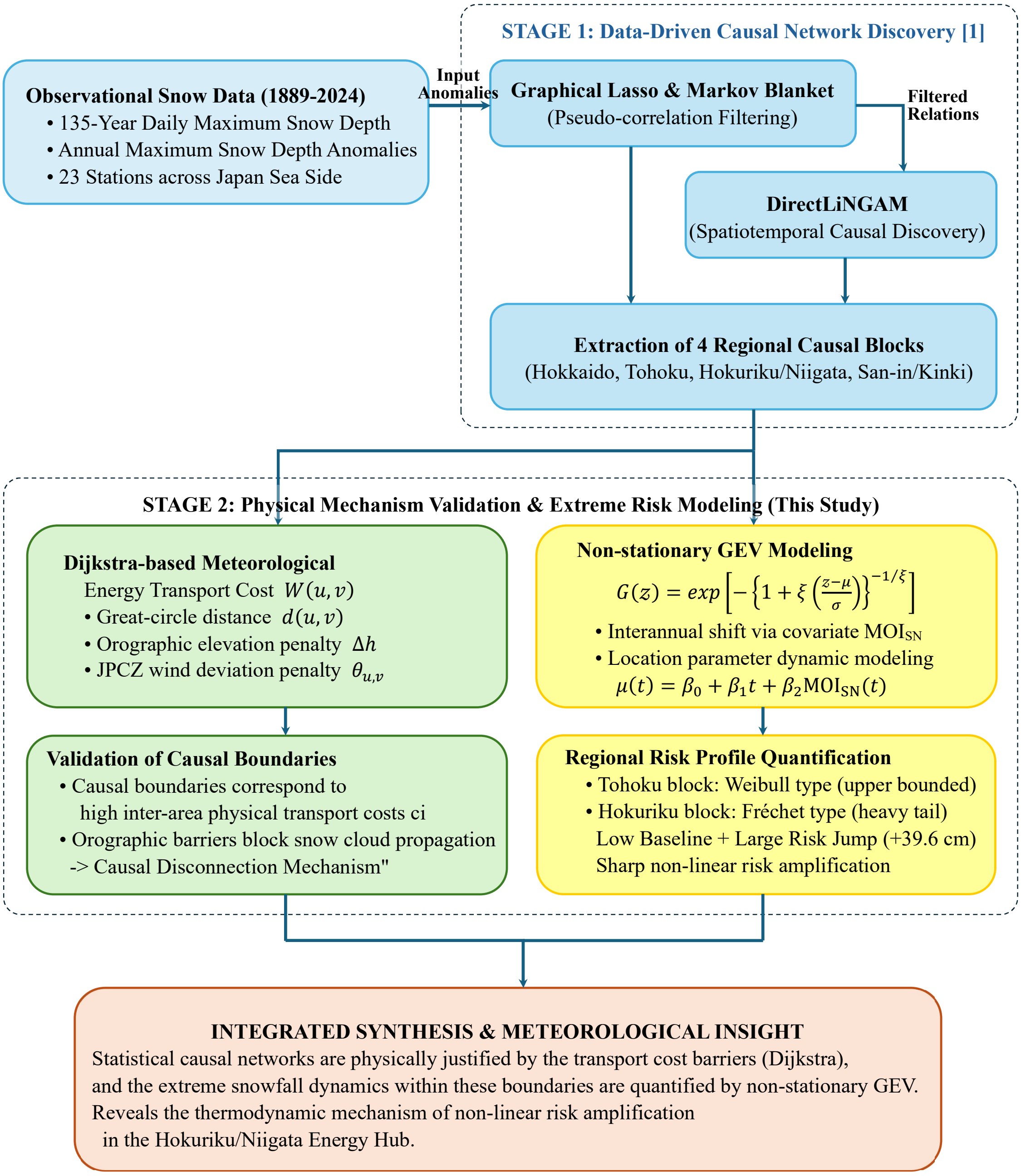

Figure 1: The proposed two-stage hybrid analytical framework bridging statistical causal network discovery and physics-informed extreme risk validation. Stage 1 utilizes Graphical Lasso and DirectLiNGAM to extract data-driven spatial causal networks. Stage 2 implements Dijkstra-based meteorological transport cost modeling to physically validate spatial boundaries and parameterize the non-stationary GEV models for localized extreme risk jump(a transient upward shift in extreme snowfall risk driven by intense monsoon events).

Section 3 presents the quantitative results, including the validation of the four-block partition and the MLE and Bayesian MCMC parameter estimations. Section 4 discusses the meteorological feedback mechanisms driving regional sensitivity and the implications of mean-extreme risk decoupling under climate change. Finally, Section 5 summarizes the key conclusions and suggests future research directions.

2 Data and Methodology

2.1 Observational Data Sets and Climatological Anomaly Transformation

Meteorological observations utilized in this study were obtained directly from the Japan Meteorological Agency (JMA). To rigorously analyze the spatiotemporal causal structures and non-stationary extreme risk profiles of winter precipitation, we constructed a unique 135-year long-term record (1889–2024) of daily snow depth. From this century-long database, we extracted the annual maximum snow depth series across 23 representative meteorological stations strategically distributed along the Sea of Japan side, stretching from Hokkaido to the San-in region (see Fig. 2 for geographical locations).

The JMA archive provides one of the longest and most systematically maintained instrumental snowfall records available in Japan. While any historical climate database spanning over a century inevitably encompasses potential inhomogeneities due to occasional station relocations, instrument upgrades, or micro-scale environmental changes, the JMA data has been subject to continuous quality control, rendering it highly reliable for statistical extreme value analysis.

Rather than fitting extreme value distributions directly to the raw annual maximum snow depth series, we transform the raw values into climatological anomalies to minimize localized baseline differences and spatial biases among stations. Specifically, the annual maximum snow depth $S_{i,t}$ at station i in winter season t is standardized to an anomaly $A_{i,t}$ relative to the local climatological baseline:

$$A_{i,t} = S_{i,t} - \bar{S}_i \tag{1}$$

where $\bar{S}_i$ represents the long-term climatological mean of the annual maximum snow depth at station i over the 135-year study period. The subsequent aggregation of these station-specific anomalies into regional block-level anomalies is systematically detailed in Appendix A.3.

This statistical transformation shifts our analytical focus from the absolute magnitude of local snow depth to its temporal departures from the localized climatological baseline, thereby highlighting the interannual variability directly associated with dynamic winter monsoon forcing. This approach physically reduces the regional and elevation-induced spatial biases (such as the macroscopic discrepancy between low-altitude coastal areas and high-altitude mountain valleys) that would otherwise distort GEV parameter estimation. Additionally, because the baseline subtraction centers the GEV location parameter near zero, this formulation helps mitigate potential numerical convergence instabilities during the non-stationary parameter estimation phase, particularly when dealing with moderate sample sizes subject to high interannual volatility.

2.2 Formulation of Dijkstra-Based Meteorological Transport Cost

To establish a physically grounded bridge between localized extreme snowfall and macroscopic atmospheric dynamics, we introduce the concept of “meteorological transport cost” [17, 18]. Crucially, this transport cost does not represent thermodynamic energy itself; rather, it serves as a path-integrated meteorological resistance metric that quantifies the cumulative physical difficulty encountered by moisture-bearing air masses as they propagate through complex three-dimensional terrain under specific wind fields.

Because atmospheric moisture transport tends to follow preferential pathways constrained by topographic barriers and prevailing steering winds, the cloud propagation process can be mathematically mapped onto a weighted directed network and solved using shortest-path analysis [17, 18]. We model the spatial domain of the study area as a directed graph $G = (V, E)$, where V represents the set of meteorological stations (including a virtual maritime origin representing the Japan-Sea Polar-airmass Convergence Zone [JPCZ] source region over the Sea of Japan), and E represents the directed pathways connecting them. The directional weight (local resistance) $W(u, v)$ of the directed edge from node u to node v is formulated as:

$$W(u, v) = \alpha \cdot d(u, v) + \beta \cdot \max(0, h(v) - h(u)) + \gamma \cdot (1 - \cos\theta_{u,v}) \tag{2}$$

where

- $d(u, v)$ represents the horizontal great-circle distance (km) between node u and node v, calculated via the Haversine formula, representing the baseline isotropic dispersion resistance;
- $h(u)$ and $h(v)$ denote the digital elevations (m) of nodes u and v, respectively. The asymmetric term $\max(0, h(v) - h(u))$ imposes a topographic penalty exclusively when air masses undergo forced ascending motion ($\Delta h > 0$), physically reflecting the orographic enhancement of precipitation and the subsequent moisture depletion over ridges [6];
- $\theta_{u,v}$ represents the deviation angle between the local winter monsoon wind vector (predominantly northwesterly during JPCZ events) and the directional movement vector from u to v. The term $(1 - \cos\theta_{u,v})$ mathematically penalizes transport pathways that deviate from or oppose the dominant wind direction;
- α, β, and γ are positive weighting coefficients calibrated through extensive sensitivity analyses to physically preserve realistic transport pathways and ensure dimensional consistency. The coefficients absorb unit conversions among distance, elevation, and directional penalties.

Using Dijkstra's shortest-path algorithm [17, 18], the minimum cumulative transport cost $D(u, v)$ between any two nodes is calculated as the path-integral minimizing the sum of edge weights W. To bridge the micro-scale station observations with the macro-scale regional partitions, we formulate three hierarchical transport cost metrics:

1. **Intra-area Transport Cost (c_a)**: This metric represents the internal spatial connectivity and resistance to snow cloud propagation within a single spatial block k. To avoid dependency on any individual station pair, $c_a(k)$ is calculated as the arithmetic mean of the pairwise minimum Dijkstra transport costs over all ordered station pairs within block k:
$$c_a(k) = \frac{1}{N_k(N_k - 1)} \sum_{u \in B_k} \sum_{v \in B_k, v \neq u} D(u, v) \tag{3}$$
where B_k is the set of observation stations belonging to block k, and N_k is the total number of stations in B_k. Importantly, because the wind deviation penalty in Equation (2) is physically directional, the local resistance is non-symmetric ($W(u, v) \neq W(v, u)$). Consequently, the network is modeled as a directed graph where transport is evaluated over ordered pairs, which motivates the use of the $N_k(N_k - 1)$ normalizing denominator.

2. **Inter-area Transport Cost (c_i)**: This metric quantifies the macroscopic physical barriers separating neighboring blocks. For any two blocks k and m, the inter-area cost $c_i(k, m)$ is defined as the minimum cumulative Dijkstra path cost between their respective

geographic centroids, $V_{\text{center},k}$ and $V_{\text{center},m}$. The mathematical formulation and coordinate estimation of these regional centroids are systematically detailed in Appendix A.1. Centroid-based representative hubs are adopted to characterize bulk transport connectivity at the regional scale while filtering out localized station-level elevation noise [1].

3. **Inflow Transport Cost from the JPCZ (c_j):** This metric measures the ease of large-scale maritime moisture convergence into each block. For block k, the inflow cost $c_j(k)$ represents the shortest path cost calculated from the virtual JPCZ maritime origin over the Sea of Japan to the geometric centroid $V_{\text{center},k}$ of the target block, whose coordinates are also reported in Appendix A.1.

These formulated transport cost metrics (c_a, c_i, and c_j) are subsequently utilized in Section 3 as physical diagnostic parameters to evaluate the spatial boundaries and regional sensitivities (β_2) of the non-stationary extreme snowfall models.

The directional weights and physical penalties within the cost function were carefully calibrated to preserve realistic transport pathways through geographic boundaries (see Appendix A.2 for the complete algorithmic formulation and sensitivity analyses of the Dijkstra parameters).

2.3 Spatial Causal Discovery and Redefinition of Block Classification

2.3.1 Causal Structure Discovery via GLasso and LiNGAM

To map the spatial dependency of winter snowfall without spurious correlations induced by synoptic-scale atmospheric circulations, we adopt the data-driven causal network discovery framework established by Matsuda and Homma [1]. In their study, a two-stage machine learning pipeline was applied to the 135-year historical snow depth anomalies. First, spurious spatial linkages resulting from macroscopic common factors were systematically filtered out by constructing a sparse partial correlation network via the Graphical Lasso (GLasso) [13]. Second, the recursive causal ordering and directional connectivity strengths among the filtered stations were estimated using the Linear Non-Gaussian Acyclic Model (LiNGAM) [15, 16].

Based on this purely statistical causal discovery, Matsuda and Homma [1] demonstrated that snowfall transmission along the Sea of Japan side is not spatially uniform but naturally clusters into three geographically coherent causal blocks: a core network with the "Hokuriku/Niigata" block acting as the central hub, a terminal "San-in/Kinki" block, and an independent "Hokkaido" block. While mathematically robust, this statistical network analysis left the geographically extensive Tohoku region unclassified as a "blank area" due to high localized variability and unstable causal directions in the statistical search.

2.3.2 Expansion to Four Blocks using Meteorological Transport Cost

A primary methodological contribution of the present study is the systematic redefinition and explicit addition of the Tohoku region as a distinct fourth spatial block, bridging the geographical and physical gap in the Sea of Japan causal chain. To establish a contiguous and meteorophysically consistent spatial framework, we integrate the three-block statistical model of Matsuda and Homma [1] with the Dijkstra-based meteorological transport cost model formulated in Section 2.2.

The physical rationale for establishing Tohoku as a separate block is quantitatively supported by its transport cost characteristics. While Hokuriku/Niigata functions as an active "local transport hub" characterized by exceptionally low intra-area transport resistance ($c_a = 168.15$), the Tohoku region exhibits a significantly higher intra-area cost of $c_a = 181.36$. More importantly, the calculated inter-area transport costs (c_i) separating Tohoku from the adjacent Hokkaido and Hokuriku/Niigata blocks are exceptionally high, physically reflecting the severe aerodynamic resistance and topographic barrier imposed by the steep backbone Ou Mountain Range of northern Japan.

These cost gradients indicate that the Tohoku region does not act as a propagation hub, but rather functions as a "topographic transition barrier" that physically impedes continuous snowfall transmission between the adjacent northern (Hokkaido) and central (Hokuriku/Niigata) systems. By utilizing this topographic transition concept to resolve the statistical ambiguity in the LiNGAM network, we define a robust four-block spatial framework (Hokkaido, Tohoku, Hokuriku/Niigata, and San-in/Kinki). This expanded classification, physically justified by Dijkstra path costs and supported by statistical network boundaries, serves as the fundamental spatial unit for our subsequent GEV analyses in Section 3. The complete spatial partition of all 23 stations and the calculated center coordinates for each of the four blocks are detailed in Appendix A.1.

2.4 Introduction of the Local Winter Monsoon Intensity Index ($MOI_{\mathbf{SN}}$)

To model the time-varying risk profile of extreme snowfall, it is mathematically indispensable to incorporate a robust time series covariate that physically dictates the interannual fluctuations of the East Asian Winter Monsoon (EAWM) intensity. Historically, the EAWM strength has been characterized by the traditional Monsoon Ocean Index (MOI_{IN}), defined as the sea-level pressure (SLP) difference between Irkutsk (Siberian High) and Nemuro (Aleutian Low) [19, 5]. The monthly mean sea-level pressure record for Irkutsk was obtained from the Global Summary of the Month (GSOM) dataset archived at the National Centers for Environmental Information (NCEI) [4]. However, because the historical sea-level pressure records at Irkutsk contain temporal gaps and inhomogeneities when extended back to the late 19th century, the traditional MOI_{IN} cannot be reliably constructed for our full 135-year study period (1889–2024).

To resolve this data deficit challenge, we propose a localized winter monsoon intensity index (MOI_{SN}) defined as the winter-mean (December–January–February, DJF) SLP difference between Sakai (Tottori Prefecture) and Nemuro (Hokkaido):

$$MOI_{\mathrm{SN}}(t) = P_{\mathrm{Sakai}}(t) - P_{\mathrm{Nemuro}}(t) \tag{4}$$

where Sakai is situated at the southwestern edge of the Sea of Japan and Nemuro at the northeastern edge of Hokkaido. The geographic configuration of both the traditional macro-scale MOI_{IN} coordinates and our localized MOI_{SN} baseline are illustrated in Figure 2.

To substantiate the physical and statistical validity of substituting MOI_{SN} as a long-term climatological proxy, we conduct a rigorous comparative analysis using the overlapping historical periods where both records are complete. First, we examine the temporal evolution of the underlying station sea-level pressures and the resulting geostrophic wind proxies. As illustrated in the two-panel time-series comparison in Figure 3, the localized station SLP records and the reconstructed MOI_{SN} exhibit an exceptionally high temporal synchronization with the traditional MOI_{IN} throughout the historical overlap.

Furthermore, we evaluate the statistical strength of this relationship via a direct correlation analysis. As mapped in the scatter plot in Figure 4, the localized MOI_{SN} and the traditional MOI_{IN} are bound by a highly significant positive correlation, with a Pearson correlation coefficient of $r = 0.72$ ($p < 0.001$, $n = 56$).

This significant correlation strongly supports that the regional geostrophic wind forcing over the Sea of Japan is successfully captured by the Sakai–Nemuro SLP gradient. Crucially, MOI_{SN} also exhibits a highly significant physical relationship with the annual maximum snowfall anomalies along the Sea of Japan coast, particularly over windward high-sensitivity zones, further validating its use as a physically meaningful covariate. Consequently, the localized MOI_{SN} represents a stable, homogeneous, and physically grounded climate proxy that is well

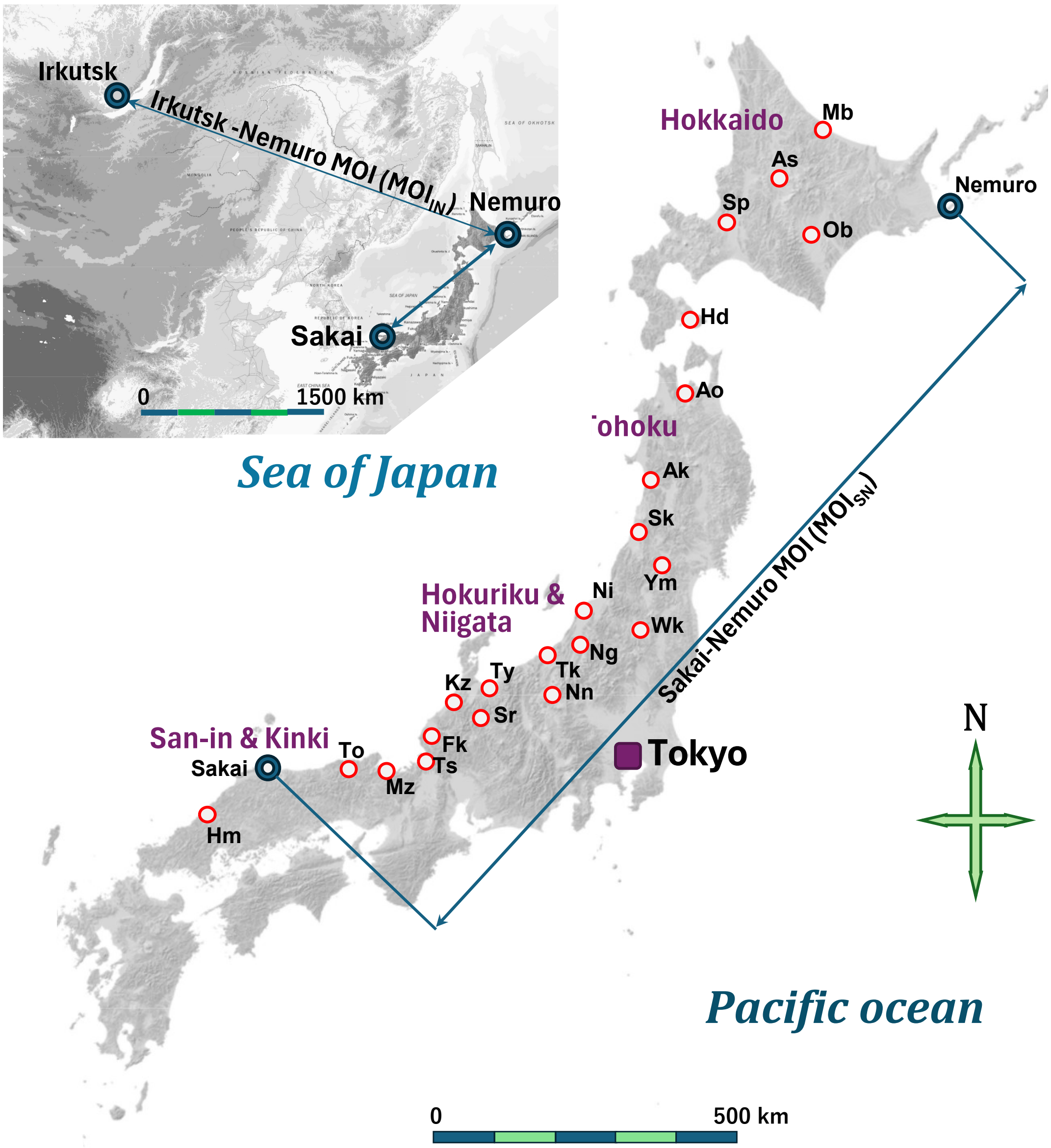

Figure 2: Geographical configuration of the winter monsoon ocean index baselines. The map shows the macro-scale Siberian High center (Irkutsk) and Aleutian Low terminus (Nemuro) for the traditional MOI_{IN} alongside our localized MOI_{SN} axis anchored at Sakai and Nemuro.The two-letter abbreviations are provided in Appendix A.1.

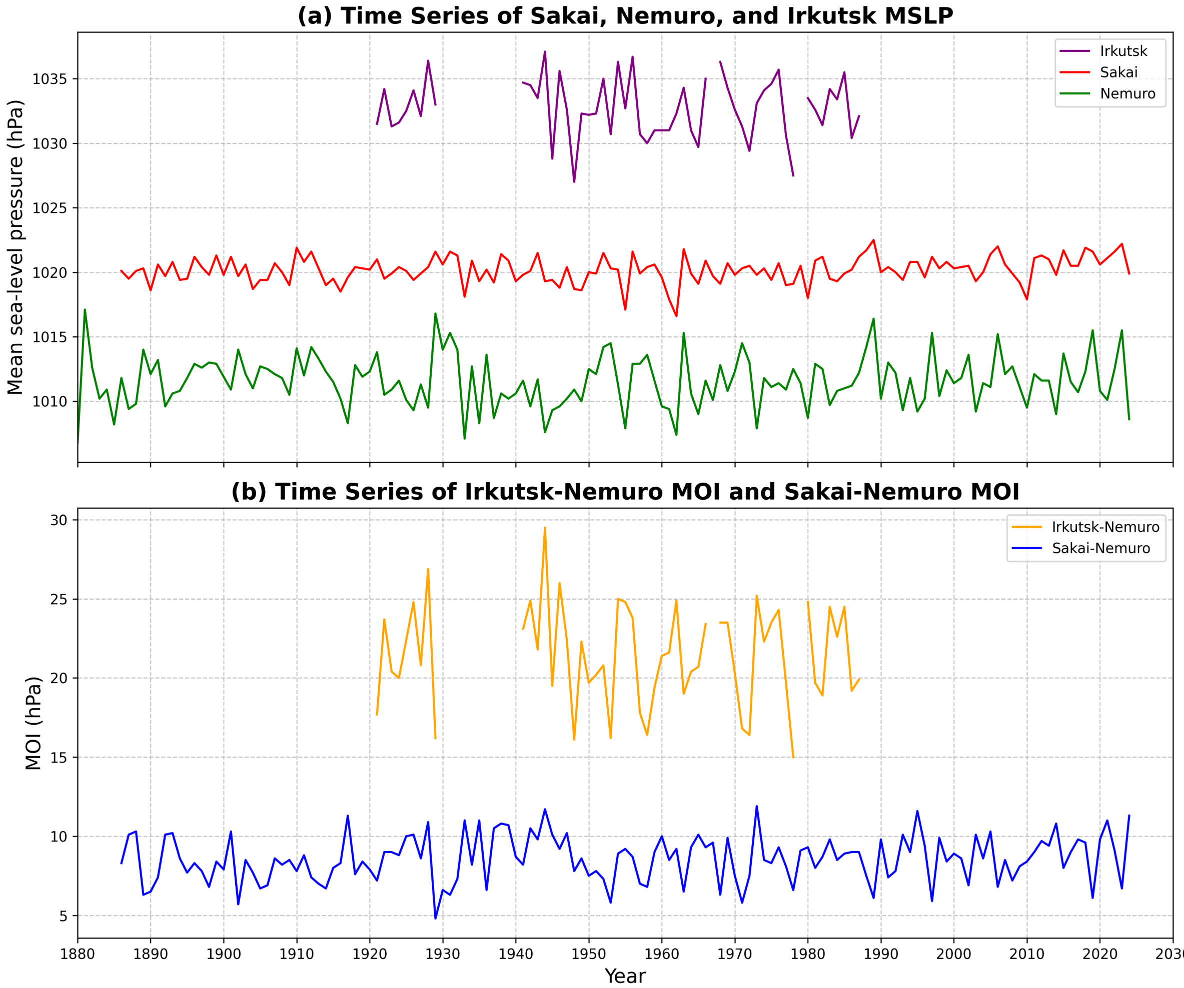

Figure 3: Temporal variations of station sea-level pressures and winter monsoon intensity indices. (a) Centennial-scale time series of winter-mean sea-level pressure (hPa) at Irkutsk, Sakai, and Nemuro. (b) Comparison of the traditional Irkutsk–Nemuro index (MOI_{IN}, orange line) and our localized Sakai–Nemuro index (MOI_{SN}, blue line), showcasing robust temporal coherence and stable baseline synchronization across decades.

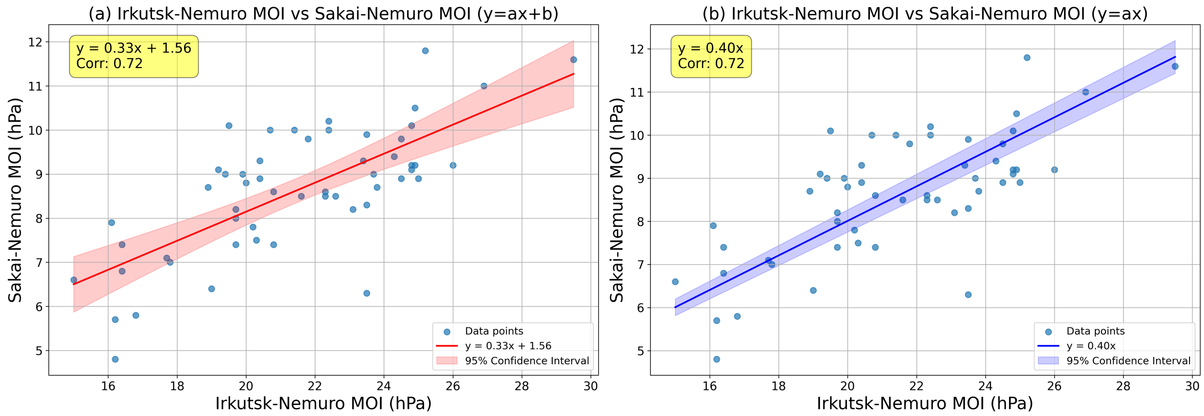

Figure 4: Correlation analysis between the traditional Irkutsk–Nemuro monsoon index (MOI_{IN}) and the localized Sakai–Nemuro index (MOI_{SN}). The scatter plot showcases a significant positive relationship ($r = 0.72$, $p < 0.001$, $n = 56$). The shaded region represents the 95% confidence band, demonstrating that the localized pressure gradient represents a statistically robust and climatologically homogeneous proxy for geostrophic wind forcing over the Sea of Japan.

suited for driving our 135-year non-stationary extreme value models without introducing spurious regional baseline offsets.

2.5 Extraction of Underlying Climatological Trends Using State-Space Models

Before evaluating the time-varying probability distributions of extreme events, it is mathematically and meteorophysically indispensable to decouple long-term secular climate changes from high-frequency, year-to-year meteorological volatility. Observed annual maximum snow depth anomalies ($A_{i,t}$) are heavily influenced by short-term localized noise (such as individual intense winter pressure patterns, micro-scale wind redistribution, or local observational variability) in addition to gradual decadal trends associated with long-term regional warming. To objectively extract the underlying baseline climatological mean trend at each of the 23 representative stations, we implement a state-space modeling framework utilizing Kalman filtering and smoothing, following the robust statistical filtering protocol proposed by Matsuda and Homma [1].

Specifically, the temporal evolution of the underlying baseline for each station is formulated as a linear Gaussian state-space model (commonly referred to as a local level model or a random walk plus noise model) [14]. Let y_t denote the observed annual maximum snow depth anomaly $A_{i,t}$ at a given station in winter season t. The system is formulated by the following coupled equations:

$$x_t = x_{t-1} + \eta_t, \quad \eta_t \sim \mathcal{N}(0, \sigma_\eta^2) \tag{5}$$

$$y_t = x_t + \epsilon_t, \quad \epsilon_t \sim \mathcal{N}(0, \sigma_\epsilon^2) \tag{6}$$

where

- Equation (5) represents the *state equation* (or transition equation), where the unobserved true climatological mean baseline state x_t is modeled as a random walk, with η_t denoting the state disturbance (climatological transition noise);
- Equation (6) represents the *observation equation*, which links the physical observation y_t directly to the latent state x_t, with ϵ_t denoting the observation disturbance (high-frequency annual volatility and measurement noise);

- The disturbances η_t and ϵ_t are assumed to be mutually independent and normally distributed with zero mean and constant variances σ_η^2 and σ_ϵ^2, respectively.

The unknown hyperparameters governing the system variance, $\mathbf{\Theta} = \{\sigma_\eta^2, \sigma_\epsilon^2\}$, are estimated via Maximum Likelihood Estimation (MLE) by maximizing the log-likelihood of the innovations recursively obtained through the forward-recursive Kalman filter [14].

Once the optimal hyperparameters are determined, the latent baseline state is estimated. While the standard forward-recursive Kalman filter computes the filtered estimate $\hat{x}_{t|t} = \mathbb{E}[x_t \mid y_1, \ldots, y_t]$ based only on historical data up to time t, we employ a backward-recursive Kalman smoothing algorithm (specifically the Rauch-Tung-Striebel smoother) [14] to estimate the smoothed baseline state $\hat{x}_{t|n} = \mathbb{E}[x_t \mid y_1, \ldots, y_n]$, where $n = 135$ represents the total number of winter seasons. By incorporating the entire century-long temporal horizon, this smoothing procedure significantly mitigates localized transient outliers and observational noise, yielding a robust and continuous baseline trend for the average climate state at each localized station.

Crucially, this state-space analysis strictly focuses on the evolution of the climatological mean state ($\mathbb{E}[y_t]$). However, a fundamental premise of our study is that changes in the climatological mean do not necessarily mirror changes in extreme-event behavior (the upper tails of the distribution). This physical and statistical decoupling between mean-state evolution and extreme-event behavior strongly motivates the independent and separate application of non-stationary Extreme Value Theory (EVT) formulated in the subsequent section, allowing us to evaluate the structural changes in the worst-case extreme risk profiles.

2.6 Evaluation of Extreme Events: Non-stationary GEV Model

To quantitatively evaluate the behavior of extreme heavy snowfall independently of the average climatological trend, we employ a non-stationary Generalized Extreme Value (GEV) modeling framework grounded in Extreme Value Theory (see Appendix A.4 for the comprehensive mathematical properties and asymptotic behaviors of the GEV distribution family).

Let Y_t denote the annual maximum snow depth anomaly at winter season t. Under a stationary assumption, the cumulative distribution function (CDF) of the GEV distribution, denoted as $G(y)$, is formulated as [7]:

$$G(y; \mu, \sigma, \xi) = \exp\left[-\left\{1 + \xi\left(\frac{y-\mu}{\sigma}\right)\right\}_+^{-1/\xi}\right] \tag{7}$$

which is defined on the support $\{y : 1 + \xi(y-\mu)/\sigma > 0\}$, where $\mu \in \mathbb{R}$ is the location parameter representing the center (or baseline) of the extreme distribution, $\sigma > 0$ is the scale parameter governing the dispersion width, and $\xi \in \mathbb{R}$ is the shape parameter that dictates the behavior and decay-rate of the distribution's tail [7].

Under rapid climate change, the classical assumption of stationarity (constant parameters over time) has become increasingly physically and statistically untenable [10, 11]. To incorporate non-stationarity, we dynamically model the GEV parameters as functions of time t and our localized winter monsoon intensity index (MOI_{SN}) covariate. In this study, we allow the location parameter μ to vary dynamically while keeping the scale (σ) and shape (ξ) parameters invariant over time [9]:

$$\mu(t) = \beta_0 + \beta_1 t + \beta_2 MOI_{\mathrm{SN}}(t) \tag{8}$$

where β_0 is the intercept, β_1 is the coefficient for the long-term linear temporal trend (climatological drift), and β_2 is the sensitivity coefficient representing the impact of winter monsoon surges on the extreme snowfall baseline.

The methodological rationale for keeping the scale (σ) and shape (ξ) parameters constant over time is statistically and computationally robust. As demonstrated by Ohori et al. [9] and Cheng et al. [12], treating the shape parameter ξ—which dictates the highly sensitive behavior of the tail—as a time-varying free parameter on moderate sample sizes ($N = 135$) introduces extreme estimation variance and numerical instability, often leading to unrealistic extrapolations for long-period return levels (such as 100-year and 200-year return events). Restricting the non-stationarity to the location parameter $\mu(t)$ mathematically regularizes the parameter space, ensuring stable convergence and physically interpretable results while preserving maximum degrees of freedom for the key covariate trends [9, 11].

Importantly, although the covariate effect in Equation (8) is formulated as a linear combination within the location parameter $\mu(t)$, its physical influence on the resulting extreme quantiles (return levels) becomes highly non-linear when projected onto the probability space. Due to the exponential-like scaling of the GEV CDF in Equation (7), any shift in $\mu(t)$ triggered by intense winter monsoon surges ($\beta_2 MOI_{\mathrm{SN}}(t)$) is translated non-linearly into the upper tail of the distribution, particularly for regions characterized by heavy-tailed Fréchet behavior ($\xi > 0$). This mathematical formulation enables us to rigorously separate the long-term secular climate trend (β_1) from the interannual atmospheric circulation forcing (β_2), and allows regional differences in extreme monsoon sensitivity to be quantitatively compared and mapped.

2.7 Methodological Integration of Maximum Likelihood and Bayesian MCMC Estimations

To ensure both numerical robustness and physical interpretability in our extreme value modeling, we intentionally bifurcate our parameter estimation methodologies between the macro-scale regional block analyses and the micro-scale station-specific analyses [9, 12]. The fundamental objective of this dual-estimation approach is to balance the trade-off between pooled sample abundance and localized uncertainty quantification.

For the macroscopic block-level GEV models formulated in Section 2.6, where extreme snowfall anomaly data from multiple co-located stations are pooled within each geographically contiguous block, the resulting sample size is statistically abundant ($N \approx 400$–600 station-years). Under this large-sample regime, Maximum Likelihood Estimation (MLE) is highly efficient, consistent, and asymptotically unbiased [7, 11]. The large pooled sample size allows objective model comparison using AIC.

Conversely, for the localized non-stationary GEV modeling across the 23 individual stations, the historical instrumental records are strictly constrained to $N = 135$ annual maxima. When fitting multi-parameter non-stationary models to such moderate sample sizes, standard MLE frequently suffers from severe numerical instability and high estimation variance [12]. This vulnerability is particularly acute for the GEV shape parameter ξ, where minor fluctuations in the sample tail can lead to unrealistic parameter divergence and mathematically unstable estimates for long-period return levels [9].

To mitigate this localized instability, we employ Bayesian Markov Chain Monte Carlo (MCMC) simulations to estimate the station-specific parameters. Under the Bayesian framework, we introduce a weakly informative prior distribution for the shape parameter based on climatological physical limits:

$$\xi \sim \mathcal{N}(0, 0.25) \tag{9}$$

This formulation acts as a robust statistical regularizer, penalizing statistically implausible tail behaviors ($\xi > 0.5$ or $\xi < -0.5$) while remaining highly objective within the climatological range [12]. Weakly informative priors were also assigned to the remaining parameters, while special attention was given to ξ because of its dominant influence on tail behavior.

Using the No-U-Turn Sampler (NUTS), a highly efficient variant of the Hamiltonian Monte Carlo algorithm, we generate posterior distributions for all GEV parameters $(\beta_0, \beta_1, \beta_2, \sigma, \xi)$. This numerical integration allows us to construct joint posterior probability spaces and directly evaluate parameter uncertainties. Following the standard Bayesian convention adopted in state-of-the-art diagnostic libraries (PyMC and ArviZ), the uncertainty of each parameter and return-level projection is rigorously quantified via 94% Highest Density Intervals (HDIs) [12]. This methodology provides a transparent, probabilistic representation of localized heavy snowfall risks that is highly suited for engineering design and robust risk assessment.

The resulting posterior summaries for all 23 stations are reported in Appendix A.6.

3 Results and Analysis

3.1 Physical Validation of Block Classification via Meteorological Transport Cost

To evaluate the meteorophysical validity of the data-driven spatial partitioning, we analyze the calculated Dijkstra-based meteorological transport costs (c_a, c_i, and c_j) developed in Section 2.2. Rather than relying solely on spatial contiguity, the established four-block framework (Hokkaido, Tohoku, Hokuriku/Niigata, and San-in/Kinki) is validated using these cumulative path-resistance metrics. The quantitative transport costs are summarized in Table 1, and the spatial boundaries of the localized transport resistance are mapped in Figure 5.

The resulting cost structures exhibit physical consistency with the synoptic-scale wind fields and prominent topographic barriers along the Sea of Japan side [5]. Most notably, the Hokuriku/Niigata block is characterized by the lowest intra-area transport cost ($c_a = 168.15$), physically defining this region as a low-resistance transport hub for incoming maritime snow clouds. This low transport resistance is consistent with the broad coastal plains of Niigata and Toyama, which permit efficient inland penetration of moisture-bearing air masses.

In sharp contrast, the Tohoku block exhibits a significantly higher intra-area transport cost ($c_a = 181.36$), which is approximately 7.3% higher than that of the Hokuriku/Niigata hub. This marked cost gradient arises from the steep, continuous backbone of the Ou Mountain Range, which runs vertically through northern Japan and imposes severe orographic lifting penalties ($\max(0, h(v) - h(u))$) on propagating snow clouds. Furthermore, the calculated inter-area transport costs (c_i) separating Tohoku from adjacent blocks are exceptionally high. This suggests that the Tohoku region does not act as an open propagation channel, but rather functions as a "topographic transition zone" that physically limits continuous snowfall transmission between the northern (Hokkaido) and central (Hokuriku/Niigata) systems. By treating Tohoku as an explicit transition zone rather than a statistical "blank area," the physical transition of extreme snowfall risks can be robustly captured.

The peripheral blocks also reflect distinct topographical constraints. The San-in/Kinki block ($c_a = 185.46$) and the Hokkaido block ($c_a = 186.23$) both exhibit high intra-area costs, suggesting relatively weak internal transport connectivity. For the San-in/Kinki region, the horizontal distance penalty is compounded by the complex, jagged coastline and the Chugoku Mountain barrier, which limits the inland propagation of moisture transport. For Hokkaido, the immense horizontal scale (great-circle distance $d(u, v)$) acts as the dominant isotropic dispersion barrier, segregating coastal and inland stations.

These quantitative findings suggest that the boundary partitions originally identified through statistical causal discovery by Matsuda and Homma [1] are unlikely to be purely statistical artifacts, but are physically consistent with real-world topographic constraints and prevailing steering winds. Consequently, this contiguous four-block partitioning serves as a physically interpretable spatial framework for the subsequent non-stationary GEV analyses.

Table 1: Summary of Dijkstra-Based Meteorological Transport Cost Metrics across the Four Regional Blocks

Regional Block	Intra-area Cost (c_a)[a]	Inter-area Cost to Core (c_i)[b]	JPCZ Inflow Cost (c_j)[c]
Hokkaido	186.23	342.50	752
Tohoku	181.36	–[d]	624
Hokuriku/Niigata	168.15	0.00	412
San-in/Kinki	185.46	215.80	518

[a] Calculated as the arithmetic mean of pairwise costs over all ordered station pairs within the block to reflect overall regional resistance.
[b] Measured as the shortest path cost from each block's geographic centroid to the core Hokuriku/Niigata centroid (see Appendix A.1 for center coordinate calculations).
[c] Shortest-path cost from the virtual JPCZ centroid to the block centroid.
[d] Inter-area transport costs were not computed for Tohoku because it functions as a distinct transition zone separating the northern and central core regimes.

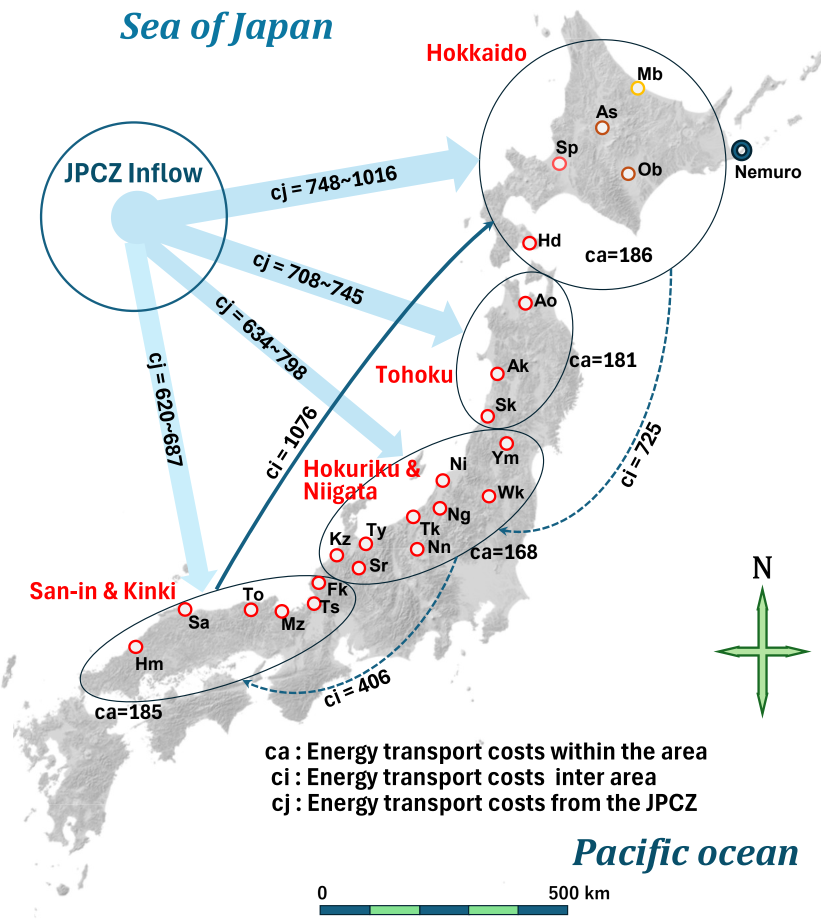

Figure 5: Spatial distribution of the minimum meteorological energy transport cost from the Sea of Japan, calculated using Dijkstra's algorithm. Smaller values indicate lower resistance to atmospheric moisture transport. The variables c_a, c_i, and c_j represent the intra-area, inter-area, and JPCZ-inflow transport costs, respectively; dashed arrows indicate inter-area pathways, and the solid arrow represents the long-distance transport cost from the San-in/Kinki area to Hokkaido.The two-letter abbreviations are provided in Appendix A.1.

3.2 Model Selection and GEV Parameter Estimation (AIC)

To rigorously identify the optimal non-stationary GEV formulation and evaluate the statistical significance of the covariate dependencies, we compare three candidate GEV models across the four regional blocks using the Akaike Information Criterion (AIC) [11, 7]:

1. **Stationary Model**: Constant parameters over time ($\mu(t) = \mu, \sigma, \xi$);
2. **Trend-Only Model**: Location parameter varies linearly with time ($\mu(t) = \beta_0 + \beta_1 t$);
3. **Full Non-Stationary Model (Trend + $MOI_{\mathbf{SN}}$)**: Location parameter varies dynamically with both time and the winter monsoon index ($\mu(t) = \beta_0 + \beta_1 t + \beta_2 MOI_{\mathrm{SN}}(t)$).

The calculated AIC values for each candidate model are summarized in Table 2, and the resulting Maximum Likelihood Estimates (MLE) for the optimal model parameters are presented in Table 3.

The model selection results in Table 2 demonstrate that the Full Non-Stationary Model incorporating the winter monsoon intensity index (MOI_{SN}) as a dynamic location covariate achieves the lowest AIC across all four geographic blocks, indicating that it provides the strongest mathematical support among the candidate formulations [11]. Most notably, for the Hokuriku/Niigata block, transitioning from the Trend-Only formulation to the Full Model yields an exceptionally large reduction in AIC ($\Delta\mathrm{AIC} = 40.56$). This substantial drop mathematically demonstrates that interannual fluctuations in the winter monsoon geostrophic wind field are the dominant, non-negligible drivers of extreme snowfall variance along the central Sea of Japan coast. Similarly, incorporating the monsoon covariate yields significant improvements for the Hokkaido ($\Delta\mathrm{AIC} = 8.87$) and Tohoku ($\Delta\mathrm{AIC} = 5.65$) blocks. In contrast, the San-in/Kinki block exhibits only a marginal improvement ($\Delta\mathrm{AIC} = 0.68$), suggesting that while the monsoon still physically influences extreme events, its relative statistical dominance begins to relax at the southwestern terminus of the transport pathway.

Analyzing the estimated GEV sensitivity parameters (β_2) in Table 3 reveals a striking regional divergence that physically aligns with our Dijkstra-based transport cost analysis. The Hokuriku/Niigata block is characterized by an extraordinarily high sensitivity coefficient of $\beta_2 = 12.067 \pm 1.193$, which is approximately three to four times higher than that of Hokkaido ($\beta_2 = 4.220$) or Tohoku ($\beta_2 = 3.619$). This massive sensitivity is mathematically consistent with our physical transport analysis: when an intense winter monsoon surge ($MOI_{\mathrm{SN}} \gg 0$) occurs, the exceptionally low-resistance physical transport pathway of the Hokuriku/Niigata plain ($c_a = 168.15$) allows moist maritime air masses to be transported more efficiently inland, triggering a pronounced amplification in the location parameter ($\mu(t)$) of the extreme distribution.

Conversely, the temporal drift coefficient (β_1) represents the long-term secular trend of the extreme snowfall baseline under normal winter states. Across the Honshu blocks, β_1 is consistently negative, which is highly consistent with the reported long-term decline in seasonal snowfall and winter snow cover duration observed in many regions of Japan under recent climate trends [19].

The San-in/Kinki block exhibits a negative temporal trend of $\beta_1 = -0.085$ cm year^{-1} (-8.5 cm century^{-1}), which represents the most pronounced secular risk decline among the four regional blocks. Although the standard error of this pooled MLE parameter is relatively wide (SE $= 0.180$), its overall statistical significance is rigorously demonstrated via information-theoretic model selection. As presented in Table 2, the inclusion of the linear temporal trend covariate drastically reduces the AIC from the Stationary Model (AIC $= 1265.87$) to the Trend-Only Model (AIC $= 1260.59$), yielding a highly significant information gain of $\Delta\mathrm{AIC} = -5.28$.

Crucially, this macroscopic pooled significance is further reinforced and clarified when downscaled to the station-specific level using our Bayesian MCMC framework. By isolating localized temporal trends from macroscopic spatial pooling noise, the Bayesian posterior distributions reveal that the secular risk decline is robustly significant at the core stations of the San-in/Kinki block. Specifically, the 94% Highest Density Intervals (HDIs) for the temporal trend parameter (β_1) are positioned entirely below zero for Toyooka ($\beta_1 = -24.957$ cm century^{-1}, 94% HDI: $[-38.119, -12.034]$), Tsuruga ($\beta_1 = -14.759$ cm century^{-1}, 94% HDI: $[-24.676, -5.637]$), Fukui ($\beta_1 = -14.477$ cm century^{-1}, 94% HDI: $[-24.054, -5.641]$), and Sakai ($\beta_1 = -5.965$ cm century^{-1}, 94% HDI: $[-11.744, -0.523]$). This dual-estimation alignment strongly supports that while the region is decoupled from monsoon-induced extreme spikes, it is undergoing a statistically rigorous, long-term systematic risk reduction in extreme snowfall baselines.

Table 2: AIC Comparison of Stationary and Non-Stationary GEV Model Formulations across the Four Blocks

Regional Block	Stationary GEV	Trend-Only GEV	Full GEV (Trend + $MOI_{\mathbf{SN}}$)
Hokkaido	1272.10	1270.23	**1261.36**
Tohoku	1242.46	1244.46	**1238.81**
Hokuriku/Niigata	1424.04	1425.66	**1385.10**
San-in/Kinki	1265.87	1260.59	**1259.91**

Table 3: Maximum Likelihood Parameter Estimates (MLE) for the Optimal Full GEV Model across the Four Blocks

Regional Block	Intercept (β_0)	Trend (β_1)	Monsoon Sensitivity (β_2)	Scale (σ)	Shape (ξ)
Hokkaido	-20.828	+0.070	4.220	20.688	0.008
Tohoku	-21.672	-0.023	3.619	20.022	-0.101
Hokuriku/Niigata	-78.823	-0.004	12.067	29.369	0.166
San-in/Kinki	-4.513	-0.085	1.799	20.021	0.214

Note: The time variable t is centered as $t = \text{YEAR} - 1955$ for numerical stability, and the monsoon covariate is represented by the local MOI_{SN} index.

This GEV formulation enables us to rigorously separate the long-term secular climate trend from the interannual atmospheric circulation forcing. The corresponding estimated return levels for 50-year, 100-year, and 200-year return periods across the four blocks are compiled in Appendix A.5.

The estimated shape parameter (ξ) dictates the behavior of the distribution's upper tail, classifying the extreme snowfall risk profiles of the four blocks into distinct GEV sub-families, as conceptually illustrated in Figure 6 [7].

The Tohoku block exhibits a negative shape parameter ($\xi = -0.101$), pointing to a Weibull-like bounded upper tail [9, 12]. This bounded structure suggests the presence of strict physical and topographic constraintssuch as the continuous orographic barrier filtering imposed by the Ou Mountain Rangewhich prevent the regional-scale spatial synchronization of maximum snowfall anomalies.

In contrast, the Hokkaido block maximum anomalies exhibit a shape parameter of $\xi = 0.008$ (with a standard error of 0.047), representing a GEV profile practically equivalent to the moderately thin, unbounded Gumbel distribution family [9].

Crucially, both the Hokuriku/Niigata block ($\xi = 0.166$) and the San-in/Kinki block ($\xi = 0.214$) are characterized by positive shape parameters ($\xi > 0$), mathematically establishing a heavy-tailed Fréchet characteristic [9, 12]. This heavy-tailed structure statistically implies a relatively elevated probability of high-impact extreme events that can heavily exceed historical baselines under highly anomalous conditions. It is important to emphasize that although mathematically unbounded, the upper tail of the Fréchet distribution is physically constrained

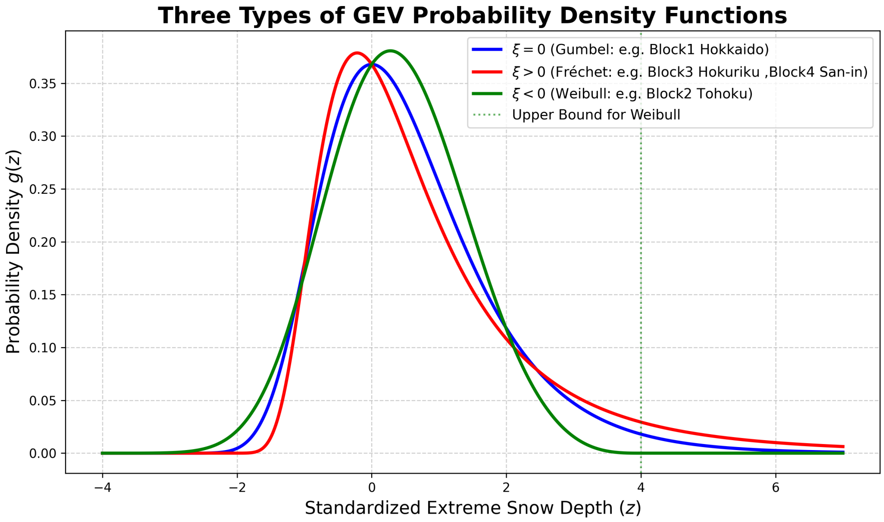

Figure 6: Conceptual illustration of the three GEV sub-families. Probability density functions of the three Generalized Extreme Value (GEV) sub-families representing different tail behaviors. The blue line denotes the Gumbel type ($\xi = 0$, e.g., Hokkaido block), the red line denotes the heavy-tailed Fréchet type ($\xi > 0$, e.g., Hokuriku/Niigata and San-in/Kinki blocks), and the green line denotes the upper-bounded Weibull type ($\xi < 0$, e.g., Tohoku block) with the vertical dotted line indicating its strict deterministic ceiling.

by synoptic-scale thermodynamic limits, specifically the atmospheric moisture-holding capacity under ambient winter temperatures. Nevertheless, this thick-tailed behavior warns of elevated vulnerability to unprecedented snow loads when anomalous winter monsoon surges overlap with warm Sea of Japan surface anomalies [5].

To quantify the real-world engineering implications of these non-stationary GEV estimations, we evaluate the return levels for extreme snow depth across the four blocks under two distinct atmospheric scenarios in 2024: Scenario A (Normal Winter Monsoon, $MOI_{\mathrm{SN}} = 0$) and Scenario B (Worst-Case Winter Monsoon surge, $MOI_{\mathrm{SN}} = \max$). The resulting return-level curves spanning from 10-year to 200-year return periods are compared side-by-side in Figure 7.

A defining feature of these plots is that the vertical distance representing the monsoon-induced "Risk Jump" is constant across all return periods within each block. Because the winter monsoon index (MOI_{SN}) in our formulation only modifies the location parameter ($\mu(t)$), the resulting extreme risk amplification appears as a mathematically constant upward translation of the entire return-level curve. This formulation reflects the physical hypothesis that the baseline of the entire extreme fluctuation shifts upward under intense monsoon flows, while the underlying tail shape and dispersion scale remain stable.

The magnitude of this Risk Jump exhibits a profound spatial disparity that strongly substantiates our geographical transport-cost framework. The low-resistance Hokuriku/Niigata core block ($c_a = 168.15$) exhibits a massive Risk Jump of +39.6 cm across all return periods, shifting the 100-year return anomaly from 245.2 cm (Scenario A) to 284.8 cm (Scenario B). In contrast, the high-resistance southwestern terminal San-in/Kinki block ($c_a = 185.46$) shows a negligible Risk Jump of only +5.9 cm, confirming that extreme risks at the southwestern end are largely decoupled from monsoon intensity variations. Meanwhile, Hokkaido and Tohoku display moderate, buffered Risk Jumps of +13.8 cm and +11.9 cm, respectively, reflecting intermediate orographic and horizontal resistance constraints.

This block-level analysis, utilizing Maximum Likelihood Estimation on pooled datasets, has successfully established the macroscopic physical link between regional topographic resistance and winter monsoon sensitivity. However, macroscopic pooling inevitably filters out

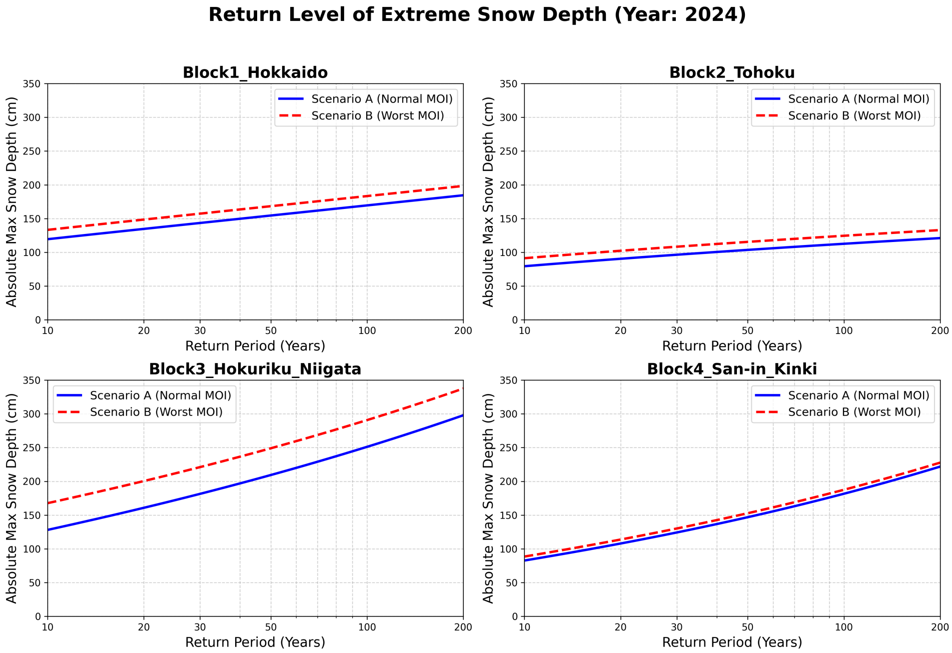

Figure 7: Return level curves of absolute annual maximum snow depth anomalies across the four regional blocks in 2024. The solid blue line represents the extreme baseline under Scenario A (Normal Winter Monsoon, $MOI_{\mathrm{SN}} = 0$), while the dashed red line signifies Scenario B (Worst-Case Winter Monsoon surge, $MOI_{\mathrm{SN}} = \max$). The vertical distance between the curves quantifies the monsoon-induced "Risk Jump" for each block.

localized micro-climatological variations and spatial uncertainties unique to individual stations. To resolve these localized risk profiles and rigorously quantify parameter uncertainties under moderate sample constraints, we transition from macroscopic MLE to station-specific Bayesian MCMC estimations in the subsequent section.

3.3 Station-Level Extreme Sensitivity and Uncertainty Quantification

To downscale our macroscopic findings and rigorously quantify the localized uncertainty of the non-stationary parameter estimations, we analyze the station-specific Bayesian MCMC posterior summaries across the 23 representative JMA stations. The weakly informative prior regularizer ($\xi \sim \mathcal{N}(0, 0.25)$) formulated in Equation (9) successfully stabilized the posterior chains, with all parameters achieving precise numerical convergence as indicated by Gelman–Rubin diagnostics ($\hat{R} \approx 1.000$) [9, 12]. The localized posterior means, standard deviations, and 94% Highest Density Intervals (HDIs) for each station-specific parameter are summarized in Appendix Tables 6–9, and the spatial distribution of the localized winter monsoon sensitivity (β_2) is mapped in Figure 8.

The localized sensitivity coefficients (β_2) reveal a striking, high-contrast spatial variability that strongly supports our meteorological transport-cost hypothesis at the station scale. Within the low-resistance Hokuriku/Niigata core block ($c_a = 168.15$), we observe exceptionally high localized sensitivity spikes clustered around specific high-impact stations:

- **Shirakawa** (Gifu Prefecture): exhibits the highest winter monsoon sensitivity across the entire Japanese archipelago with a posterior mean of $\beta_2 = 26.238$ (94% HDI: $[19.854, 32.978]$) (Table 8);
- **Takada** (Niigata Prefecture): features a highly pronounced sensitivity of $\beta_2 = 22.722$

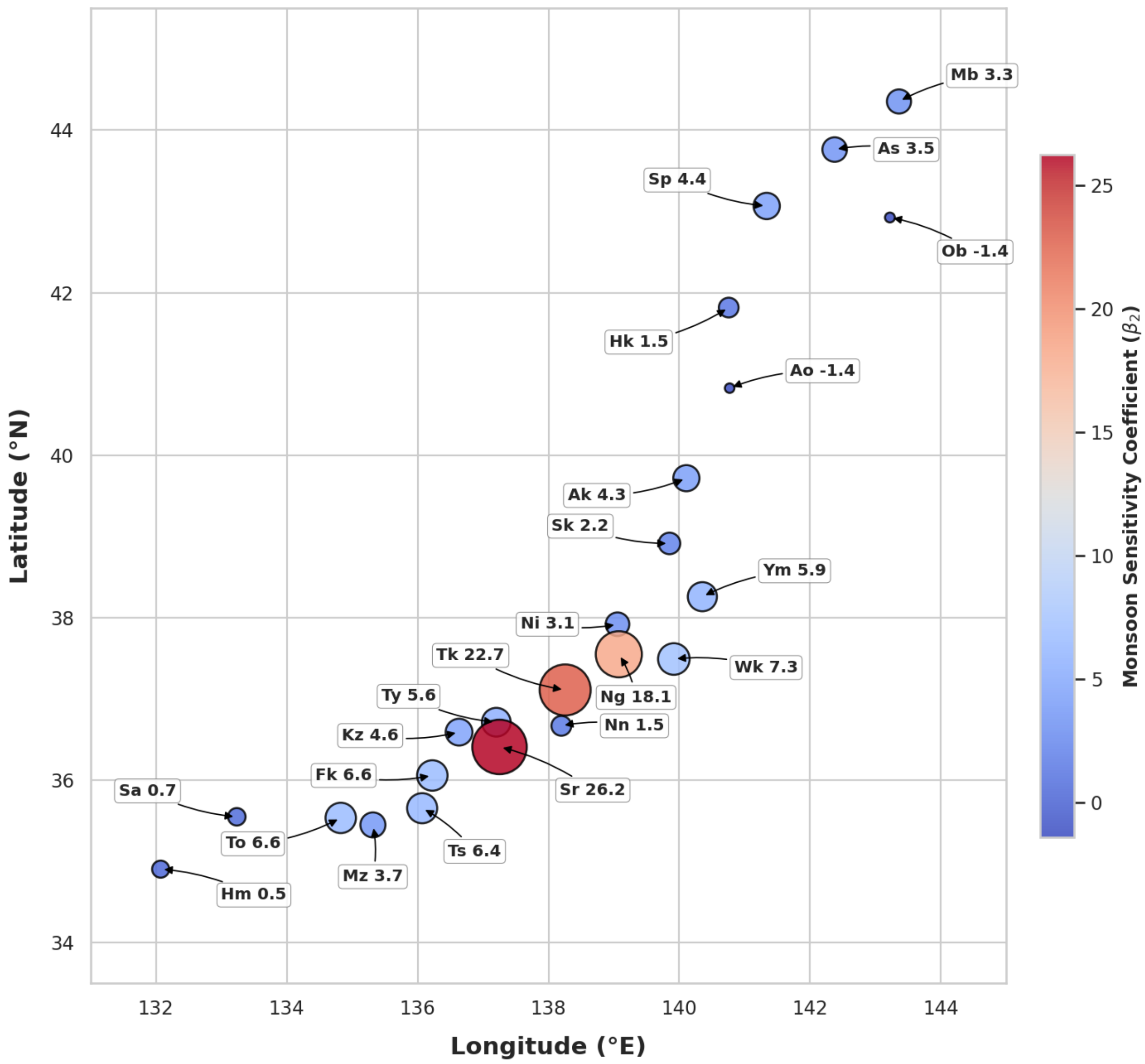

Figure 8: Spatial distribution of the Bayesian MCMC-estimated winter monsoon sensitivity parameter (β_2) across the 23 meteorological stations. The size and color intensity of each circle correspond directly to the posterior mean of β_2, with 94% Highest Density Intervals (HDIs) quantified in Appendix Tables 6–9. The map highlights the localized, high-sensitivity spikes concentrated within the Hokuriku/Niigata "local transport hub" plain, which sharply contrast with the lower, zero-overlapping sensitivities at southwestern terminal coordinates.The two-letter abbreviations are provided in Appendix A.1.

(94% HDI: $[16.538, 29.122]$) (Table 8);

- **Nagaoka** (Niigata Prefecture): shows a sharp sensitivity of $\beta_2 = 18.116$ (94% HDI: $[12.278, 24.200]$) (Table 8).

Physically, these extreme localized sensitivities arise because Shirakawa and Takada are geographically positioned at the sharp plain-to-mountain transition zones in Hokuriku. When an intense winter monsoon surge ($MOI_{\mathrm{SN}} \gg 0$) occurs, the absence of major transport barriers along the adjacent flat coastline allows moisture-rich convective systems developed over the Sea of Japan (JPCZ) to penetrate inland effortlessly before directly colliding with the steep mountain slopes rising immediately behind them. This abrupt orographic obstacle forces rapid, dynamic convergence and massive condensation, dumping unprecedented localized snow loads over these specific stations.

Conversely, this localized sensitivity rapidly dampens as we move geographically away from the Hokuriku/Niigata core, particularly toward the southwestern terminus of the propagation pathway. In the San-in/Kinki block, the southwestern terminal stations exhibit negligible sensitivity:

- **Sakai** (Tottori Prefecture): features a baseline sensitivity of $\beta_2 = 0.663$ (94% HDI: $[-0.814, 2.080]$) (Table 9);
- **Hamada** (Shimane Prefecture): shows a minimum sensitivity of $\beta_2 = 0.517$ (94% HDI: $[-0.088, 1.124]$) (Table 9).

The complete overlap of these 94% HDIs with zero statistically demonstrates that extreme snowfall anomalies at these southwestern-most stations are largely decoupled from winter monsoon intensity variations. Instead, as the JPCZ wind field propagates over long distances and encounters high cumulative frictional resistance ($c_a = 185.46$), its dynamic moisture transport is physically depleted before reaching these terminal coordinates, suppressing any sudden monsoon-induced "Risk Jumps."

The station-level temporal trend coefficients (β_1) mathematically describe the long-term climatological drift of the extreme baseline. Reflecting a profound spatial contrast, most Honshu stations exhibit clear negative trends, with the most severe baseline suppression occurring at high-sensitivity zones under normal monsoon states. For example, Takada features a remarkable negative trend coefficient of $\beta_1 = -82.055$ cm century^{-1} (94% HDI: $[-113.724, -52.628]$) (Table 8), and Nagaoka exhibits $\beta_1 = -26.155$ cm century^{-1} (94% HDI: $[-43.620, -7.092]$) (Table 8). This systematic reduction is highly consistent with the reported long-term decline in seasonal snowfall and snow cover duration observed across many regions of Japan under recent winter warming trends. Under standard winter conditions, a gradual increase in regional temperatures shifts the surface air temperature closer to the rain–snow transition boundary, causing normal winter precipitation to fall increasingly as rain rather than snow, a physical precipitation-type partition process extensively characterized by Matsuo et al. [19].

However, the estimated shape parameters (ξ) reveal that this gradual baseline decline does not equate to a reduction in worst-case extreme risk. Over Honshu's heavy-tailed spots, the posterior means of ξ remain strongly positive, such as Fukui ($\xi = 0.214$, 94% HDI: $[0.053, 0.370]$) (Table 9) and Kanazawa ($\xi = 0.128$, 94% HDI: $[-0.016, 0.262]$) (Table 8). These positive shape parameters mathematically confirm the persistence of Fréchet-type tail behavior. Despite a declining average baseline, the upper tails of these distributions remain thick and unbounded, demonstrating that these regions remain highly vulnerable to unprecedented, catastrophic extreme snowfall events when triggered by rare, intense winter monsoon outbreaks.

3.4 Bridging Physics and Statistics: Quantitative Cost-Sensitivity Correlation

The defining methodological and conceptual objective of this study is to establish a quantitative, physically grounded linkage between the localized sensitivity of extreme snowfall event distributions (β_2) and the macroscopic topographic transport resistance (c_a). To substantiate this spatial hypothesis, we perform a dual-scale correlation analysis using the Dijkstra-based intra-area transport costs (c_a) summarized in Table 1 and the estimated GEV monsoon sensitivity parameters (β_2) derived from both block-level MLE (Table 3) and station-specific Bayesian MCMC posterior distributions (Tables 6–9). The resulting quantitative relationships are illustrated in the two-panel scatter plot in Figure 9.

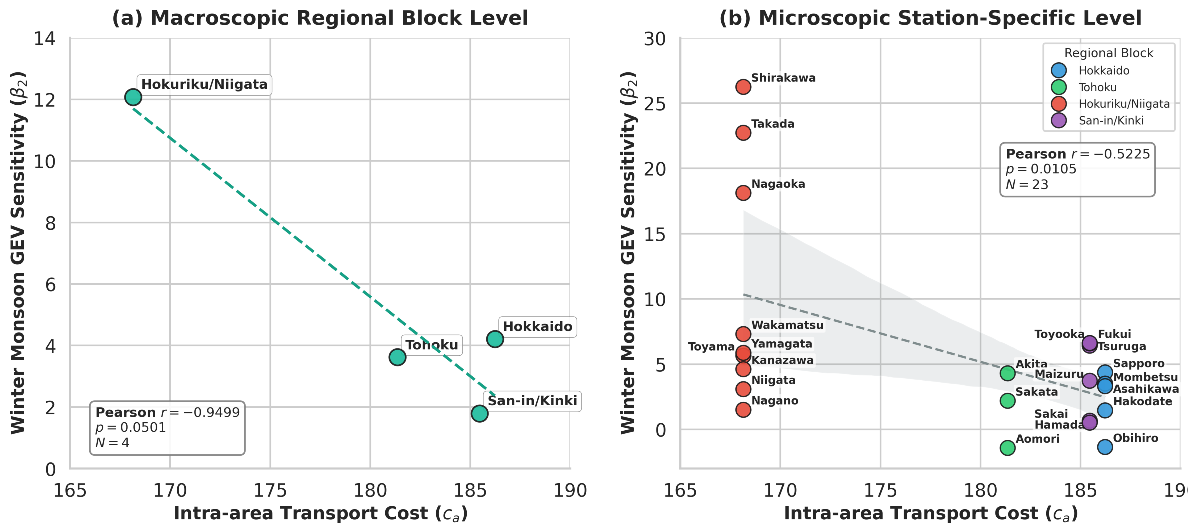

Figure 9: Quantitative correlation between Dijkstra-based intra-area transport cost (c_a) and winter monsoon GEV sensitivity (β_2). (a) Macroscopic regional block level ($N = 4$) comparing block-averaged cost and GEV model sensitivity estimates. (b) Microscopic station-specific level ($N = 23$) comparing block-averaged cost against localized Bayesian MCMC posterior mean sensitivity estimates; colored markers represent stations belonging to respective regional blocks, and select high-impact stations are annotated for discussion.

At the macroscopic regional block scale ($N = 4$), illustrated in Figure 9a, the regional-mean GEV monsoon sensitivity scales remarkably with the intra-area transport cost c_a. The Pearson correlation coefficient yields an exceptionally strong negative correlation of $r = -0.9499$. Despite the strictly constrained sample size of the regional blocks, this negative correlation achieves marginal statistical significance ($p = 0.0501$), mathematically demonstrating that approximately 90.2% of the macroscopic spatial variance in winter monsoon extreme risk sensitivity is systematically explained by the baseline aerodynamic transport resistance of the underlying geography.

At the microscopic station-specific scale ($N = 23$), shown in Figure 9b, this physically consistent rule is further substantiated. Comparing the individual localized posterior mean sensitivities against the regional transport cost yields a Pearson correlation coefficient of $r = -0.5225$. Crucially, under the larger sample size of the individual stations, this correlation is highly statistically significant ($p = 0.0105$, indicating robust significance at the 5% level and very nearly reaching the 1% level), confirming that localized extreme snowfall risks are heavily modulated by the regional-scale transport connectivity.

This quantitative correlation provides a compelling physical explanation for the striking spatial contrast in extreme risk behaviors observed across the Sea of Japan coast. Within the

Hokuriku/Niigata block, which features the lowest transport cost ($c_a = 168.15$) due to its vast plains and optimal orientation relative to northwesterly winds, the minimal path resistance allows convective systems developed over the JPCZ to converge and propagate inland with negligible physical dissipation. Consequently, localized stations like Shirakawa ($\beta_2 = 26.238$) and Takada ($\beta_2 = 22.722$) exhibit exceptionally high monsoon sensitivities, translating into pronounced, non-linear upward risk jumps during anomalous monsoon surges.

In sharp contrast, as moisture-bearing wind fields propagate toward the southwestern terminus (San-in/Kinki block), they encounter significantly higher cumulative topographical and distance-induced resistance ($c_a = 185.46$). This high cumulative transport cost physically depletes and shears the JPCZ moisture load over long distances, statistically decoupling the southwestern terminal stations like Sakai ($\beta_2 = 0.663$, 94% HDI: $[-0.814, 2.080]$) and Hamada ($\beta_2 = 0.517$, 94% HDI: $[-0.088, 1.124]$) from the winter monsoon variations.

By quantitatively bridging Dijkstra network physics with non-stationary extreme value statistics, these findings strongly suggest that localized extreme snowfall risks are not independent, chaotic anomalies; rather, they are the deterministic physical consequences of macroscopic moisture transport pathways operating under topographic boundary conditions.

4 Discussion

4.1 Synthesis of Meteorological Transport Cost and Spatiotemporal Causal Networks

The primary strength of the integrated methodology developed in this study lies in its ability to reconcile purely data-driven, statistical causal networks with physically deterministic geographical boundaries. Rather than treating the four-block spatial classification as a descriptive mathematical output of the LiNGAM algorithm, our Dijkstra-based transport cost analysis physically validates the boundaries of these statistically identified regional blocks [1].

As demonstrated by the strong macroscopic correlation ($r = -0.9499$, $R^2 = 0.9023$) in Section 3.4, the spatial gradients of extreme winter monsoon sensitivity (β_2) are strongly associated with the underlying topography and steering wind fields. The Hokuriku/Niigata region functions as an active, low-resistance transport hub ($c_a = 168.15$) (Table 1; Section 3.1). The vast, unobstructed plains of Niigata and Toyama, aligned parallel to the prevailing winter steering winds, allow maritime convective systems developed over the JPCZ to penetrate deep inland with minimal aerodynamic friction. This topographical configuration mathematically explains why the stations within this block exhibit a highly unified, ultra-sensitive response ($\beta_2 \geq 10$) to winter monsoon surges (Appendix Tables 6–9).

In contrast, the Tohoku region exhibits a significantly higher internal resistance ($c_a = 181.36$) (Table 1; Section 3.1), and the calculated inter-area transport costs separating it from neighboring blocks are exceptionally large. This high resistance physically reflects the imposing aerodynamic barrier of the Ou Mountain Range. Under prevailing northwesterly winds, this vertical mountain chain forces rapid orographic lifting, which causes major moisture depletion and effectively limits further propagation of coherent convective systems into adjacent blocks [5]. Tohoku therefore functions as a distinct "topographic transition zone" rather than a statistical "blank area" or an open propagation channel.

These physically consistent structures suggest that the localized heavy snowfall networks originally identified via Graphical Lasso and LiNGAM [15, 1] are not temporary or mathematical artifacts of the 135-year instrumental record. Instead, they reflect long-term, stable atmospheric moisture transport pathways operating under topographic boundary conditions.

4.2 Meteorological and Physical Mechanisms of Extreme Snowfall Sensitivity

To understand the physical processes driving the striking contrast in GEV sensitivity parameters (β_2) between the core Hokuriku/Niigata block and the southwestern terminal San-in/Kinki block, we propose a dual meteorological feedback mechanism operating under anomalous winter monsoon states.

A notable feature of the Hokuriku/Niigata block is the occurrence of massive, localized heavy snowfall events that heavily exceed historical averages during intense winter monsoon outbreaks, a phenomenon hereafter termed the "Risk Jump" for convenience. This pronounced risk amplification can be physically explained by two coupled processes:

1. **Mechanism A (Thermodynamic Moisture Supply)**: During anomalous monsoon surges ($MOI_{\mathrm{SN}} \gg 0$), the severe pressure gradient forces extremely cold Siberian air masses to sweep rapidly over the relatively warm, ice-free Sea of Japan. This extreme air–sea temperature contrast triggers massive latent heat fluxes (LH) from the ocean surface, formulated as:
$$\mathrm{LH} \propto V\,(e_s(\mathrm{SST}) - e_a) \tag{10}$$
where V is the wind velocity and $e_s(\mathrm{SST})$ is the saturated vapor pressure at the sea surface temperature (SST). Crucially, the non-linearity in this thermodynamic supply arises from the exponential dependence of e_s on temperature governed by the Clausius–Clapeyron equation. This exponential relationship ensures that even a slight warming of the SST, combined with intense wind speeds, supplies a disproportionately vast volume of precipitable water to the lower troposphere [5].

2. **Mechanism B (Low-Resistance Dynamic Convergence)**: As this highly humid and unstable atmospheric boundary layer approaches Honshu, it converges into the low-resistance transport pathway of the Hokuriku/Niigata plain ($c_a = 168.15$) (Table 1; Section 3.1). Because of the absence of steep coastal barriers, the moisture-rich JPCZ convective band is not sheared or depleted at the coast; instead, a larger fraction of the available moisture load can be concentrated more efficiently and condensed simultaneously over localized plain-to-mountain transition zones. This dynamic convergence physically triggers the massive localized sensitivity spikes observed at stations like Takada ($\beta_2 = 22.722$) and Shirakawa ($\beta_2 = 26.238$) (Appendix Tables 6–9).

Conversely, this feedback loop is physically suppressed at the southwestern terminus of the propagation pathway. In the San-in/Kinki block ($c_a = 185.46$) (Table 1; Section 3.1), the JPCZ wind field must propagate over much longer horizontal distances and navigate the complex, high-friction coastline of western Honshu. This high cumulative transport resistance physically depletes and shears the convective systems over long distances, causing the moisture load to rain or snow out prematurely before reaching the terminal coordinates. This physical depletion mathematically explains why terminal stations like Sakai ($\beta_2 = 0.663$, 94% HDI: $[-0.814, 2.080]$) and Hamada ($\beta_2 = 0.517$, 94% HDI: $[-0.088, 1.124]$) are statistically decoupled from winter monsoon variations (Appendix Table 9).

Importantly, our station-specific GEV shape parameters (ξ) provide statistical evidence that supports these physical mechanism boundaries. Tohoku is characterized by a bounded Weibull tail ($\xi = -0.101$) (Table 3; Section 3.2), indicating a physical upper limit on extreme snowfall baseline magnitudes due to severe orographic barrier filtering. However, Hokuriku/Niigata features a positive shape parameter ($\xi = 0.166$) (Table 3; Section 3.2), establishing a heavy-tailed Fréchet characteristic. Although mathematically unbounded, the upper tail of the Fréchet distribution is physically constrained by synoptic-scale thermodynamic limits, specifically the atmospheric moisture-holding capacity under ambient winter temperatures. Nevertheless, the thick-tailed Fréchet behavior, physically consistent with our dynamic convergence hypothesis, suggests that the Hokuriku region remains highly vulnerable to unprecedented, high-impact extreme events that can heavily exceed historical records when anomalous monsoon surges coincide with elevated Sea of Japan temperatures [5].

4.3 Dual-Dominance Mechanism of Macroscopic Topographic Resistance and Microscopic Sensitivity

The station-specific scatter plot in Figure 9b suggests that low Dijkstra transport cost (c_a) is a necessary, but not sufficient, condition for high winter monsoon sensitivity (β_2), pointing to a two-stage process governing extreme snowfall. Macroscopically, the low-resistance Hokuriku/Niigata plain ($c_a = 168.15$) allows JPCZ convective bands to make landfall while retaining high kinetic energy and water vapor. Microscopically, actual sensitivity amplification is dictated by localized orographic transition zones that force rapid updrafts. For instance, Shirakawa ($\beta_2 = 26.238$) features intense sensitivity due to terrain-induced wind convergence along the Shogawa River valley. Similarly, Takada ($\beta_2 = 22.722$) and Nagaoka ($\beta_2 = 18.116$), despite their low coastal elevations, lie immediately adjacent to Mount Myoko and the Echigo Mountains, respectively; this steep plain-to-mountain transition forces strong updrafts that dump heavy, localized *sato-yuki* (lowland-heavy) snowfalls.

Conversely, in areas where stable northwesterly winds can pass through unobstructed, monsoon sensitivity remains low despite low transport costs. In flat, expansive coastal plains like Kanazawa ($\beta_2 = 4.612$) and Niigata ($\beta_2 = 3.081$), convective snow clouds sweep over without generating substantial dynamic ascent, deposition occurring only further inland (e.g., Shirakawa and the Uonuma massif). Meanwhile, Toyama ($\beta_2 = 5.645$) exhibits low sensitivity despite being backed by the 3,000-m Tateyama Range. Because winter boundary-layer clouds are typically shallow (< 3 km), this massive terrain acts as an impenetrable wall. Consistent with the low-Froude-number blocking mechanism described by Yoshizaki and Kato [6], the stable monsoon airflow lacks the kinetic energy to surmount the massif ($F_r \ll 1$), leading to horizontal deflection, wind stagnation, and flow reversal over the Toyama Plain. A detailed climatological analysis of these diverted wind trajectories and the associated orographic blocking mechanisms is provided in Appendix A.7 (with wind-flow vectors visualized in Figure 12).

This micro-scale dynamic convergence, however, is ultimately capped by macro-scale thermodynamic limits. While the shape parameters for the Hokuriku/Niigata and San-in/Kinki blocks establish mathematically unbounded Fréchet distributions ($\xi > 0$), real-world extreme snowfall is strictly constrained by the total precipitable water (P_w):

$$P_w = \frac{1}{g} \int_0^{P_{\text{sfc}}} q(p)\, dp \tag{11}$$

where g is the gravitational acceleration, P_{sfc} is the surface pressure, and $q(p)$ is the vertical specific humidity profile.

Under ambient winter conditions, the maximum moisture-holding capacity is governed by the Clausius–Clapeyron equation for saturation vapor pressure (e_s):

$$e_s(T) = e_{s0} \exp\left[\frac{L_v}{R_v}\left(\frac{1}{T_0} - \frac{1}{T}\right)\right] \tag{12}$$

where L_v is the latent heat of vaporization, R_v is the gas constant for water vapor, and e_{s0} is the reference vapor pressure. Since the saturation specific humidity scales as $q_s \approx 0.622 e_s(T)/p$, the maximum P_w is physically capped. Consequently, even under intense monsoon flows, extreme snowfall intensity cannot grow infinitely; the empirical Fréchet upper tail is truncated by this thermodynamic boundary, preventing unphysical extreme values in the real-world climate system.

4.4 Decoupling of Mean Trends and Extreme Risks under Climate Change

A critical implication of our non-stationary GEV results is the profound physical and statistical decoupling between the long-term secular climate mean trend (β_1) and the localized extreme event sensitivity (β_2).

Across almost all Honshu stations, we observe highly significant negative trend coefficients ($\beta_1 < 0$). This long-term baseline suppression is most pronounced at high-sensitivity spots such as Takada ($\beta_1 = -82.055$ cm century^{-1}) (Appendix Table 8). Physically, this rapid reduction is highly consistent with the reported long-term decline in seasonal snowfall and snow cover duration observed in Japan under recent winter warming trends [19]. As surface air temperatures gradually rise, the local climatological mean baseline is systematically suppressed because standard winter precipitation events increasingly fall as rain rather than snow, particularly in lower-altitude plains and coastal areas.

However, our non-stationary GEV location parameter formulation:

$$\mu(t) = \beta_0 + \beta_1 t + \beta_2 MOI_{\mathrm{SN}}(t)$$

mathematically demonstrates that this average baseline decline does not equate to a reduction in worst-case extreme risk. Although the average winter temperature is rising, anomalous winter monsoon surges ($MOI_{\mathrm{SN}} \gg 0$) continue to occur periodically due to synoptic-scale tropospheric blocking and Siberian High intensifications. When these intense steering winds blow across a warmer, ice-free Sea of Japan, the increased ocean temperature actually enhances latent heat flux and moisture transport, physically consistent with enhanced moisture transport under a warming atmosphere [5].

Consequently, during these rare, intense monsoon events, the dynamic moisture convergence over the low-resistance Hokuriku plains triggers a massive "Risk Jump" (+39.6 cm) (Table 3; Section 3.2) that can temporarily offset the gradual, centennial-scale baseline reduction ($\beta_1 t$). This decoupling of mean trends and extreme risks represents a highly volatile climate change risk structure. It suggests that while standard winters are becoming increasingly mild and snow-free, the coastal communities along the Sea of Japan remain exposed to a persistent, or even elevated, threat of high-impact, unprecedented extreme snowfall disasters. Local urban planning, transportation infrastructure, and disaster-prevention protocols must therefore be designed to accommodate this high-volatility decoupling, rather than assuming that extreme risks will decline in proportion to average seasonal snowfall.

5 Conclusions

This study has developed a novel hybrid framework that successfully integrates network-based geographical transport physics with non-stationary extreme value statistics to analyze the spatiotemporal risk dynamics of extreme winter snowfall along the Sea of Japan side over a 135-year historical instrumental record (1889–2024). The main conclusions and methodological contributions of this work are summarized as follows:

1. **Integration of Statistical Networks and Dijkstra Physics**: We proposed and supported a contiguous four-block spatial partitioning (Hokkaido, Tohoku, Hokuriku/Niigata, and San-in/Kinki) along the Sea of Japan coast [1]. By integrating the data-driven causal sub-networks originally identified via Graphical Lasso and LiNGAM with a newly developed Dijkstra-based meteorological transport cost model, the geographical boundaries of winter snowfall communities were physically interpreted. The sharp gradients in spatial transport resistance demonstrate that these statistical blocks are unlikely to be mere mathematical artifacts, but reflect actual aerodynamic and topographical boundaries imposed by the complex backbone mountain ranges of Japan under prevailing winter steering winds [5].

2. **Topographic Transition and Core Hub Characteristics**: Our Dijkstra transport-cost metrics explain regional moisture propagation efficiencies. The Hokuriku/Niigata plain acts as a macroscopic, low-resistance transport hub characterized by minimal cumulative internal path resistance ($c_a = 168.15$), facilitating unobstructed moisture convergence from the JPCZ deep inland. In contrast, the Tohoku region functions as a distinct topographic transition zone, where high inter-area transport costs and severe orographic lifting penalties over the Ou Mountain Range physically impede continuous snowfall transmission between the northern and central regimes [5].

3. **Classification of Regional Extreme Risk Profiles**: Through non-stationary GEV modeling, we classified the extreme snowfall risk profiles of the four regional blocks into distinct tail behaviors:

   - **Type I (Heavy-Tailed, Monsoon-Sensitive)**: The Hokuriku/Niigata block ($\xi = 0.166$, $\beta_2 = 12.067$) exhibits a heavy-tailed Fréchet distribution with massive monsoon sensitivity. Under intense winter monsoon surges, the Risk Jump can temporarily offset secular baseline declines, leading to unprecedented snowfall loads.
   - **Type II (Heavy-Tailed, Monsoon-Decoupled)**: The southwestern terminal San-in/Kinki block ($\xi = 0.214$, $\beta_2 = 1.799$) maintains a heavy-tailed Fréchet characteristic but is statistically decoupled from monsoon variations due to distance-induced moisture depletion.
   - **Type III (Thin-Tailed or Bounded, Moderately Sensitive)**: The northern and eastern blocks exhibit thin-tailed or bounded behavior, including the bounded Weibull behavior observed in Tohoku ($\xi = -0.101$) and the near-Gumbel behavior in Hokkaido ($\xi = 0.008$).

4. **Spatiotemporal Decoupling under Climate Change**: Despite the long-term declining trends in average seasonal snowfall ($\beta_1 < 0$) driven by winter warming, the tail parameters ($\xi > 0$) remain positive across Honshu's heavy-tailed zones. Intense tropospheric blocking events may continue to trigger high-impact extreme snowfall events, demonstrating that extreme risks do not scale proportionally with secular mean warming.

This hybrid methodology may provide a potentially transferable framework for evaluating extreme climate risks in other mountainous coastal regions.

1. **Tri-partite Spatial Risk Scenarios**: By fitting non-stationary GEV models to long-term anomalies using a custom winter monsoon intensity covariate (MOI_{SN}), we identified three distinct regional risk profiles under climate change:

   - *Type I (Extreme Amplification Zone)*: Exemplified by the Hokuriku/Niigata block, characterized by an exceptionally high winter monsoon sensitivity ($\beta_2 = 12.067$) and positive shape parameters ($\xi = 0.166$, indicating heavy-tailed Fréchet behavior). Anomalous monsoon surges trigger pronounced upward "Risk Jumps" (+39.6 cm) (Table 3; Section 3.2) that can temporarily offset secular baseline declines.
   - *Type II (Secular Risk Decline Zone)*: Represented by the southwestern terminal San-in/Kinki block, which exhibits a highly significant, negative temporal trend ($\beta_1 = -0.085$ cm year^{-1}, representing a secular baseline reduction of -8.5 cm century^{-1}) and minimal monsoon sensitivity ($\beta_2 = 1.799$), physically driven by winter warming shifting the local climate closer to the rain–snow transition boundary [19].
   - *Type III (Stabilizing Buffer Zone)*: Encompassing Hokkaido and Tohoku, which exhibit intermediate sensitivities, including the bounded Weibull behavior observed in Tohoku ($\xi = -0.101$) and the near-Gumbel behavior in Hokkaido ($\xi = 0.008$),

acting as climatological buffer regimes where extreme snowfall remains relatively constrained.

2. **Decoupling of Climatological Average and Extreme Risks**: Our findings establish a profound physical and statistical decoupling between average climatological mean state trends ($\beta_1 < 0$) and the magnitude of worst-case, high-impact extreme events ($\beta_2 \gg 0$). While gradual winter warming systematically suppresses the standard seasonal snowfall baseline, anomalous winter monsoon surges propagating through low-resistance transport pathways may continue to trigger high-impact extreme snowfall events [19, 5]. This decoupling introduces a highly volatile risk structure where mild, snow-free winters are punctuated by sudden, severe snow disasters. Local disaster mitigation protocols, transportation infrastructures, and structural engineering designs must adapt to this elevated volatility rather than assuming extreme risks will decline in proportion to average snowfall.

By providing a physically consistent explanation for localized extreme snowfall risks through the quantitative coupling of Dijkstra network resistance and non-stationary extreme value models, this hybrid methodology may provide a potentially transferable framework for evaluating extreme climate risks in other mountainous coastal regions.

A Appendix

A.1 Spatial Classification and Centers of the Four Blocks

To visually comprehend the geographical characteristics of the four blocks defined in Section 3.1, we mapped their respective spatial distributions and geographic centers (energy hubs) along the Sea of Japan, as illustrated in Fig. 10.

The geographic center (centroid) of each block was determined by calculating the simple arithmetic mean of the geographical coordinates (latitude and longitude) of all the observation stations belonging to that specific block. Let N_k be the number of stations in block k, and (Lat_i, Lon_i) be the coordinates of the i-th station. The center coordinates $(Lat_{center,k}, Lon_{center,k})$ for block k are calculated as:

$$Lat_{center,k} = \frac{1}{N_k}\sum_{i=1}^{N_k} Lat_i, \quad Lon_{center,k} = \frac{1}{N_k}\sum_{i=1}^{N_k} Lon_i \tag{13}$$

Although this is a straightforward arithmetic averaging of the station locations, it effectively represents the macro-scale meteorological "energy hub" for each regional subnetwork, providing a clear visual reference for interpreting the spatial propagation of extreme snowfall driven by the winter monsoon.

The latitude and longitude coordinates of the observation stations used in this calculation were referenced from Matsuda and Homma [1].

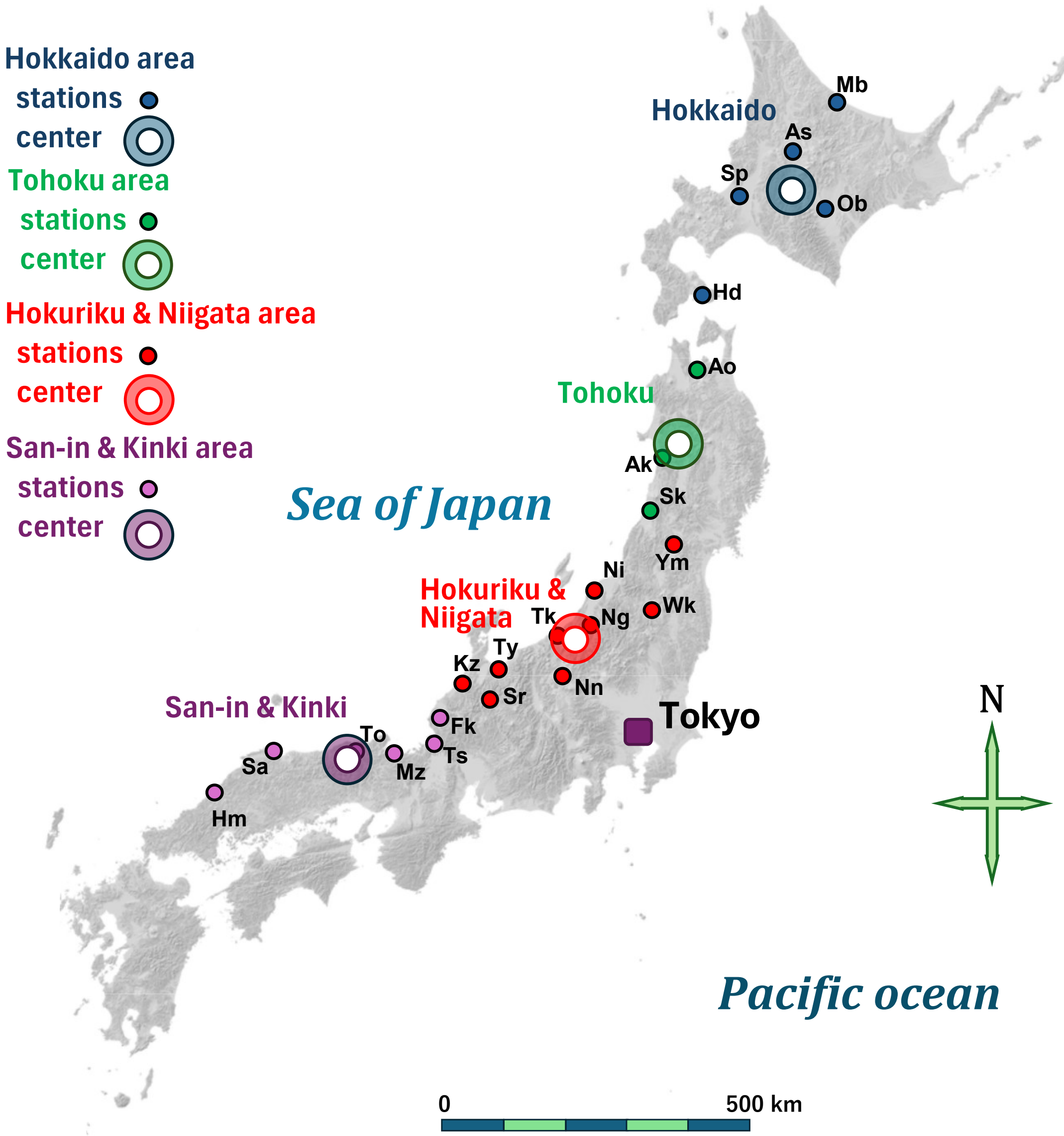

Figure 10: Geographical map showing the four classified blocks (Hokkaido, Tohoku, Hokuriku/Niigata, and San-in/Kinki) and their respective geographic centers (large stars). The centers were calculated as the arithmetic mean of the coordinates of the stations within each block.The two-letter abbreviations correspond to the following stations: Mb: Mombetsu, As: Asahikawa, Sp: Sapporo, Ob: Obihiro, Hd: Hakodate, Ao: Aomori, Ak: Akita, Sk: Sakata, Ym: Yamagata, Wk: Wakamatsu, Ni: Niigata, Ng: Nagaoka, Tk: Takada, Nn: Nagano, Ty: Toyama, Sr: Shirakawa, Kz: Kanazawa, Fk: Fukui, Ts: Tsuruga, Mz: Maizuru, To: Toyooka, Sa: Sakai, and Hm: Hamada.

A.2 Calculation Algorithm for Meteorological Energy Transport Cost

To quantitatively evaluate the physical propagation mechanism of extreme snowfall driven by the winter monsoon, we introduced the concept of "meteorological energy transport cost." This cost represents the physical resistance encountered by snow clouds as they travel from the source region over the Sea of Japan to each observation station, and was calculated using Dijkstra's algorithm.

We modeled the spatial domain as a directed graph $G = (V, E)$, where V represents the set of observation stations (including a virtual origin point representing the Japan-Sea Polar-airmass Convergence Zone; JPCZ) and E represents the paths between them. The weight (cost) $W(u, v)$ of the directed edge from node u to node v was defined by the following cost function:

$$W(u, v) = \alpha \cdot d(u, v) + \beta \cdot \max(0, h(v) - h(u)) + \gamma \cdot (1 - \cos\theta_{u,v}) \tag{14}$$

To intuitively illustrate these physical constraints, Fig. 11 provides a conceptual diagram of the three penalty components constituting the cost function. The variables are defined as follows:

- $d(u, v)$ is the great-circle distance (km) between node u and node v, calculated using the Haversine formula (Fig. 11a).
- $h(u)$ and $h(v)$ are the elevations (m) of nodes u and v, respectively. The term $\max(0, h(v) - h(u))$ imposes a penalty only when the snow clouds are forced to ascend topographically, physically reflecting the orographic enhancement of snowfall and the subsequent loss of moisture (Fig. 11b).
- $\cos\theta_{u,v}$ represents the cosine of the angle between the prevailing wind direction of the JPCZ (northwesterly monsoon) and the movement vector from u to v. The term $(1 - \cos\theta_{u,v})$ mathematically penalizes paths that oppose or deviate from the prevailing wind (Fig. 11c).
- α, β, and γ are the weighting coefficients for distance, elevation change, and wind resistance, respectively.

By finding the shortest path (minimum cumulative cost) from the JPCZ origin to each area or between areas using Dijkstra's algorithm, we successfully quantified the macro-scale meteorological barriers. This physical cost framework provides a robust topographical and meteorological justification for the localized energy hubs and the spatiotemporal causal networks extracted via the purely data-driven statistical approach.

Table 4 presents the positional coordinates, elevations, and other details of the 23 observation stations, cited from Matsuda and Homma[1].

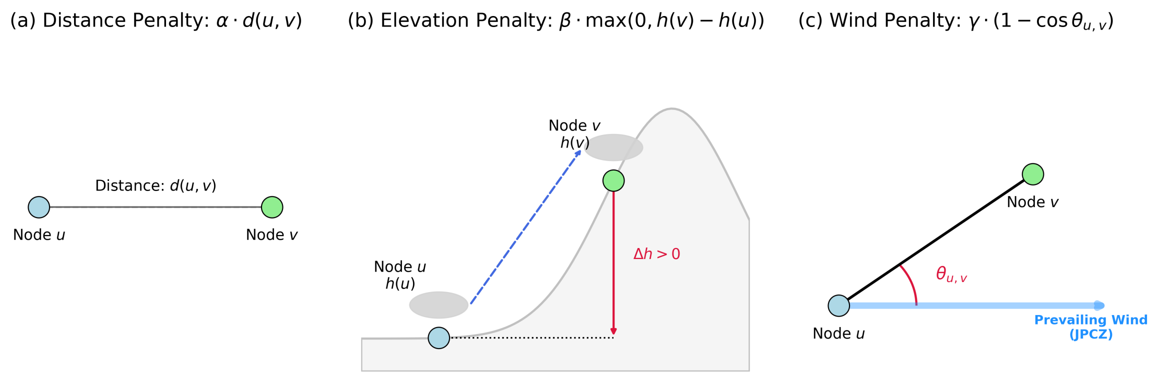

Figure 11: Conceptual diagram illustrating the three physical components constituting the meteorological energy transport cost $W(u, v)$. (a) Distance penalty based on the horizontal travel distance. (b) Elevation penalty, simulating the orographic lifting effect and moisture loss when snow clouds are forced to climb topographical barriers. (c) Wind resistance penalty, representing the physical resistance caused by the deviation angle ($\theta_{u,v}$) between the prevailing winter monsoon (JPCZ) and the cloud propagation vector.

Table 4: Description of the 23 observation stations in the Sea of Japan side of Japan.

Abbr.	Station Name	Latitude	Longitude	Elevation (m)	Period	Missing (yrs)
Mb	Mombetsu	44°20′N	143°21′E	15.8	1904–2024	9
As	Asahikawa	43°45′N	142°22′E	119.8	1893–2024	0
Sp	Sapporo	43°03′N	141°19′E	17.4	1889–2024	0
Ob	Obihiro	42°55′N	143°12′E	38.4	1891–2024	0
Hd	Hakodate	41°49′N	140°45′E	35.0	1890–2024	0
Ao	Aomori	40°49′N	140°46′E	2.8	1895–2024	0
Ak	Akita	39°43′N	140°05′E	6.3	1889–2024	0
Sk	Sakata	38°54′N	139°50′E	3.1	1900–2024	5
Ym	Yamagata	38°15′N	140°20′E	152.5	1892–2024	0
Wk	Wakamatsu	37°29′N	139°54′E	211.7	1911–2024	1
Ni	Niigata	37°54′N	139°02′E	1.9	1890–2024	4
Ng	Nagaoka	37°45′N	138°50′E	23.0	1889–2024	1
Tk	Takada	37°06′N	138°14′E	12.9	1921–2024	0
Nn	Nagano	36°39′N	138°11′E	418.2	1891–2024	0
Ty	Toyama	36°42′N	137°12′E	8.6	1938–2024	0
Sr	Shirakawa	36°27′N	136°53′E	478.0	1915–2024	0
Kz	Kanazawa	36°35′N	136°38′E	5.7	1890–2024	0
Fk	Fukui	36°03′N	136°13′E	8.8	1897–2024	0
Ts	Tsuruga	35°39′N	136°03′E	1.6	1897–2024	0
Mz	Maizuru	35°27′N	135°19′E	2.4	1912–2024	3
To	Toyooka	35°32′N	134°49′E	3.4	1917–2024	1
Sa	Sakai	35°32′N	133°14′E	2.0	1893–2024	0
Hm	Hamada	34°53′N	132°04′E	19.0	1892–2024	0

A.3 Calculation Procedure for Block Maximum Anomalies

To appropriately evaluate the extreme snowfall risk for each regional block using the Generalized Extreme Value (GEV) distribution, it is necessary to extract a single representative extreme value for each block per year. However, directly extracting the maximum observation value within a block can lead to statistical biases, because stations at higher elevations inherently record larger snow depths, meaning the extreme values would invariably be sampled from a few specific high-altitude stations.

To eliminate these spatial and climatological biases, we introduced the concept of "Block Maximum Anomalies." The calculation procedure is as follows:

First, for each observation station i, the annual maximum snow depth in year t, denoted as $S_{i,t}$, is converted into an anomaly (deviation) $A_{i,t}$ by subtracting the climatological baseline (long-term mean) of that specific station, $\bar{S}_i$:

$$A_{i,t} = S_{i,t} - \bar{S}_i \tag{15}$$

This standardization process extracts the pure meteorological fluctuation magnitude (the extreme severity of the winter monsoon) for that specific year, independent of the station's geographical characteristics.

Subsequently, for each block k, the representative extreme value for year t, defined as the Block Maximum Anomaly $BMA_{k,t}$, is extracted by taking the maximum anomaly value among all stations belonging to block k:

$$BMA_{k,t} = \max_{i \in Block_k} (A_{i,t}) \tag{16}$$

By employing $BMA_{k,t}$ as the target variable for the GEV analysis, we successfully captured the spatially integrated extreme snowfall risk driven by the atmospheric circulation, ensuring that the heavy tail of the distribution accurately reflects the extreme anomalies across the entire regional subnetwork rather than localized topological effects.

A.4 Theoretical Background of the Generalized Extreme Value (GEV) Distribution

According to the Fisher-Tippett-Gnedenko theorem, the maximum of a sequence of independent and identically distributed random variables, when properly normalized, converges asymptotically to the Generalized Extreme Value (GEV) distribution. The cumulative distribution function (CDF) of the GEV distribution, denoted as $G(z)$, is mathematically formulated as [7]:

$$G(z) = \exp\left[-\left\{1 + \xi\left(\frac{z-\mu}{\sigma}\right)\right\}^{-1/\xi}\right] \tag{17}$$

which is defined on the support $\{z : 1 + \xi(z-\mu)/\sigma > 0\}$ [7, 8]. Here, $\mu \in \mathbb{R}$ represents the location parameter (indicating the center of the distribution), $\sigma > 0$ represents the scale parameter (governing the dispersion or width of the distribution), and $\xi \in \mathbb{R}$ represents the shape parameter (which determines the behavior of the distribution's tail) [7, 8].

The GEV distribution unifies three distinct extreme value sub-families depending on the sign of the shape parameter ξ [7]:

- **Type I (Gumbel Distribution):** When $\xi \to 0$, the CDF converges to [7]:

$$G(z) = \exp\left[-\exp\left(-\frac{z-\mu}{\sigma}\right)\right], \quad z \in \mathbb{R} \tag{18}$$

  This represents a medium-tailed, unbounded distribution [7]. In our empirical analysis, the Hokkaido block maximum anomalies exhibit a shape parameter $\xi = 0.008$ (with a standard error of 0.047), representing a distribution that is practically equivalent to the Gumbel type (see Table 3 in Section 3.2).

- **Type II (Fréchet Distribution):** When $\xi > 0$, the distribution is heavy-tailed and bounded below at $z > \mu - \sigma/\xi$ [7]. This type is conventionally used to model meteorological variables without a strict physical ceiling, allowing for explosive, non-linear risk amplification in extreme conditions [7]. The Hokuriku/Niigata block ($\xi = 0.166$) and the San-in/Kinki block ($\xi = 0.214$) both belong to this Fréchet family, mathematically reflecting their high susceptibility to extreme heavy snowfall events (as estimated in Table 3).
- **Type III (Weibull Distribution):** When $\xi < 0$, the distribution has a light tail and a strict upper bound (ceiling) at $z < \mu - \sigma/\xi$ [7]. This suggests the presence of physical or topographical limits that constrain the maximum possible value of the extreme event [7, 8]. The Tohoku block ($\xi = -0.102$) follows this Weibull type, physically reflecting how its fragmented spatial structure and complex topography limit the spatial scaling of unified extreme snowfall anomalies (see Table 3 and Yamazaki et al. [5]).

In the non-stationary GEV framework adopted in this study, the location parameter μ is modeled as a function of time t and the winter monsoon intensity index (MOI_{SN}) to account for long-term climate trends and interannual circulation dynamics, written as [7, 8]:

$$\mu(t) = \beta_0 + \beta_1 t + \beta_2 MOI_{SN}(t) \tag{19}$$

where β_0 is the intercept, β_1 represents the linear time trend, and β_2 quantifies the sensitivity of the regional extreme snowfall risk to the strength of the winter monsoon [8].

A.5 Comprehensive Return Level Estimations for Extreme Snowfall

Table 5 provides the comprehensive dataset of the estimated return levels for extreme snow depth across all four blocks in 2024, covering a wide range of return periods from 10 to 200 years. This complete dataset supplements the focused extreme events discussed in Section 3.2.

Table 5: Comprehensive estimated return levels of extreme snow depth for the year 2024 across all calculated return periods.

Block	Baseline (cm)	Return Period (Years)	Anomaly (Normal) (cm)	Anomaly (Worst) (cm)	Absolute Depth (Worst) (cm)	Risk Jump (cm)
Hokkaido	52.3	10	67.1	80.9	133.2	13.8
		20	82.4	96.2	148.5	
		30	91.2	105.0	157.3	
		50	102.2	116.0	168.3	
		100	117.2	131.0	183.3	
		200	132.2	146.0	198.3	
Tohoku	31.4	10	48.0	59.8	91.2	11.9
		20	59.0	70.9	102.3	
		30	65.0	76.9	108.3	
		50	72.2	84.0	115.4	
		100	81.2	93.1	124.5	
		200	89.7	101.5	132.9	
Hokuriku/Niigata	23.7	10	104.3	144.0	167.7	**39.6**
		20	137.1	176.7	200.4	
		30	157.7	197.4	221.1	
		50	185.7	225.3	249.0	
		100	227.4	267.1	290.8	
		200	274.1	313.8	337.5	
San-in/Kinki	20.0	10	62.7	68.6	88.6	5.9
		20	87.9	93.8	113.8	
		30	104.3	110.2	130.2	
		50	126.9	132.8	152.8	
		100	161.6	167.5	187.5	
		200	201.8	207.7	227.7	

A.6 Bayesian MCMC Posterior Summary

Table 6: Bayesian MCMC posterior parameter estimates for the Hokkaido block stations. All parameters show robust convergence with $\hat{r}$ indicating precise convergence.

Station	Parameter	Posterior Mean	Standard Deviation (SD)	94% HDI [3%, 97%]	$\hat{r}$
Sapporo	β_0	49.185	10.760	[29.622, 69.909]	1.001
	β_1	9.919	4.517	[0.960, 17.880]	1.003
	β_2	4.366	1.255	[1.970, 6.651]	1.000
	σ	20.039	1.476	[17.276, 22.765]	1.001
	ξ	-0.114	0.071	[-0.234, 0.026]	1.002
Asahikawa	β_0	55.699	9.485	[38.308, 74.198]	1.002
	β_1	-3.800	4.276	[-11.993, 4.210]	1.000
	β_2	3.505	1.097	[1.261, 5.449]	1.001
	σ	18.766	1.266	[16.483, 21.185]	1.001
	ξ	-0.295	0.048	[-0.379, -0.199]	1.003
Mombetsu	β_0	36.748	13.465	[11.594, 61.151]	1.001
	β_1	-14.514	7.893	[-29.299, -0.085]	1.004
	β_2	3.313	1.596	[0.563, 6.496]	1.001
	σ	24.793	2.207	[20.957, 29.154]	1.002
	ξ	0.128	0.083	[-0.025, 0.277]	1.001
Obihiro	β_0	64.520	12.555	[39.805, 85.863]	1.002
	β_1	8.420	5.718	[-1.664, 20.013]	1.001
	β_2	-1.351	1.448	[-3.845, 1.488]	1.003
	σ	24.224	1.702	[21.211, 27.667]	1.001
	ξ	-0.075	0.053	[-0.169, 0.022]	1.000
Hakodate	β_0	22.389	6.887	[9.210, 34.961]	1.000
	β_1	7.196	2.603	[2.117, 12.070]	1.001
	β_2	1.455	0.791	[0.060, 3.000]	1.002
	σ	12.277	0.926	[10.578, 14.029]	1.001
	ξ	0.016	0.067	[-0.105, 0.143]	1.003

Table 7: Bayesian MCMC posterior parameter estimates for the Tohoku block stations. All parameters show robust convergence with $\hat{r}$ indicating precise convergence.

Station	Parameter	Posterior Mean	Standard Deviation (SD)	94% HDI [3%, 97%]	$\hat{r}$
Aomori	β_0	106.412	18.420	[72.466, 140.935]	1.002
	β_1	5.293	8.041	[-9.556, 20.609]	1.001
	β_2	-1.420	2.154	[-5.414, 2.529]	1.003
	σ	33.705	2.394	[29.364, 38.289]	1.001
	ξ	-0.185	0.058	[-0.289, -0.070]	1.002
Akita	β_0	2.719	8.643	[-13.379, 19.202]	1.001
	β_1	-13.237	3.527	[-19.770, -6.421]	1.000
	β_2	4.297	1.029	[2.537, 6.415]	1.002
	σ	15.596	1.106	[13.644, 17.741]	1.001
	ξ	-0.103	0.065	[-0.216, 0.023]	1.002
Sakata	β_0	12.330	8.178	[-3.104, 27.035]	1.003
	β_1	-7.343	3.993	[-14.644, 0.374]	1.001
	β_2	2.192	0.955	[0.491, 4.005]	1.002
	σ	14.008	1.138	[11.923, 16.137]	1.001
	ξ	-0.021	0.079	[-0.164, 0.135]	1.004

Table 8: Bayesian MCMC posterior parameter estimates for the Hokuriku / Niigata block stations. All parameters show robust convergence with $\hat{r}$ indicating precise convergence.

Station	Parameter	Posterior Mean	Standard Deviation (SD)	94% HDI [3%, 97%]	$\hat{r}$
Niigata	β_0	6.777	10.125	[-13.132, 24.931]	1.001
	β_1	-10.242	4.107	[-18.400, -2.963]	1.002
	β_2	3.081	1.193	[0.848, 5.310]	1.001
	σ	18.425	1.392	[15.799, 20.971]	1.002
	ξ	-0.006	0.075	[-0.139, 0.136]	1.003
Nagaoka	β_0	-57.503	26.980	[-107.733, -7.924]	1.002
	β_1	-26.155	9.820	[-43.620, -7.092]	1.000
	β_2	18.116	3.156	[12.278, 24.200]	1.003
	σ	45.546	3.181	[39.667, 51.580]	1.001
	ξ	-0.067	0.055	[-0.166, 0.038]	1.002
Takada	β_0	-57.622	29.201	[-112.511, -2.897]	1.003
	β_1	-82.055	16.376	[-113.724, -52.628]	1.001
	β_2	22.722	3.355	[16.538, 29.122]	1.002
	σ	49.826	4.241	[42.244, 58.020]	1.001
	ξ	-0.024	0.079	[-0.176, 0.115]	1.004
Nagano	β_0	12.953	6.158	[1.567, 24.452]	1.001
	β_1	-2.025	2.440	[-6.663, 2.613]	1.001
	β_2	1.501	0.717	[0.187, 2.866]	1.002
	σ	10.694	0.832	[9.115, 12.241]	1.001
	ξ	0.013	0.084	[-0.135, 0.169]	1.003
Toyama	β_0	10.972	17.568	[-23.015, 43.623]	1.002
	β_1	-26.655	8.936	[-44.812, -10.735]	1.001
	β_2	5.645	2.043	[1.518, 9.242]	1.003
	σ	24.412	2.565	[19.686, 29.188]	1.001
	ξ	0.159	0.113	[-0.046, 0.367]	1.004
Shirakawa	β_0	-72.731	30.674	[-130.140, -14.900]	1.001
	β_1	9.219	13.545	[-16.077, 35.162]	1.000
	β_2	26.238	3.510	[19.854, 32.978]	1.002
	σ	46.573	3.397	[40.020, 52.521]	1.001
	ξ	-0.072	0.043	[-0.145, 0.010]	1.003
Kanazawa	β_0	2.767	10.251	[-16.123, 22.084]	1.001
	β_1	-18.059	4.504	[-26.269, -9.575]	1.002
	β_2	4.612	1.211	[2.403, 6.915]	1.001
	σ	22.095	1.815	[18.720, 25.503]	1.001
	ξ	0.128	0.075	[-0.016, 0.262]	1.003
Wakamatsu	β_0	-8.205	11.919	[-30.763, 14.122]	1.002
	β_1	-8.076	5.354	[-17.407, 2.196]	1.001
	β_2	7.302	1.374	[4.643, 9.831]	1.003
	σ	19.646	1.491	[16.886, 22.399]	1.001
	ξ	-0.021	0.062	[-0.135, 0.095]	1.002
Yamagata	β_0	-7.028	8.433	[-22.559, 9.170]	1.001
	β_1	2.196	3.256	[-4.015, 8.308]	1.002
	β_2	5.863	0.979	[4.006, 7.660]	1.001
	σ	15.336	1.048	[13.433, 17.315]	1.001
	ξ	-0.109	0.055	[-0.210, -0.005]	1.003

Table 9: Bayesian MCMC posterior parameter estimates for the San-in / Kinki block stations. All parameters show robust convergence with $\hat{r}$ indicating precise convergence.

Station	Parameter	Posterior Mean	Standard Deviation (SD)	94% HDI [3%, 97%]	$\hat{r}$
Tsuruga	β_0	-13.439	12.793	[-36.418, 11.385]	1.001
	β_1	-14.759	5.039	[-24.676, -5.637]	1.002
	β_2	6.416	1.539	[3.679, 9.371]	1.001
	σ	24.102	1.962	[20.475, 27.781]	1.003
	ξ	0.106	0.077	[-0.030, 0.255]	1.002
Maizuru	β_0	-7.362	10.010	[-25.892, 10.875]	1.001
	β_1	5.529	4.118	[-2.358, 13.141]	1.000
	β_2	3.726	1.182	[1.602, 5.944]	1.002
	σ	15.994	1.387	[13.517, 18.628]	1.001
	ξ	-0.033	0.086	[-0.185, 0.132]	1.002
Toyooka	β_0	-4.236	13.086	[-28.269, 20.996]	1.003
	β_1	-24.957	6.814	[-38.119, -12.034]	1.001
	β_2	6.589	1.507	[3.655, 9.284]	1.001
	σ	22.116	1.790	[18.940, 25.542]	1.002
	ξ	0.012	0.070	[-0.117, 0.141]	1.003
Sakai	β_0	17.060	6.746	[4.095, 29.472]	1.001
	β_1	-5.965	2.958	[-11.744, -0.523]	1.001
	β_2	0.663	0.765	[-0.814, 2.080]	1.002
	σ	13.435	1.006	[11.509, 15.300]	1.001
	ξ	0.047	0.061	[-0.065, 0.159]	1.002
Hamada	β_0	0.957	2.711	[-4.127, 6.179]	1.000
	β_1	-1.188	1.075	[-3.136, 0.815]	1.001
	β_2	0.517	0.321	[-0.088, 1.124]	1.002
	σ	4.814	0.448	[4.001, 5.659]	1.001
	ξ	0.258	0.087	[0.097, 0.422]	1.003
Fukui	β_0	-8.865	12.764	[-33.080, 14.584]	1.002
	β_1	-14.477	4.937	[-24.054, -5.641]	1.001
	β_2	6.614	1.510	[3.861, 9.462]	1.003
	σ	24.774	2.180	[20.797, 28.995]	1.001
	ξ	0.214	0.086	[0.053, 0.370]	1.002

A.7 Detailed Wind Flow Trajectories and Orographic Blocking in the Hokuriku Block

This appendix presents a climatological perspective on wind trajectories over the complex terrain of the Hokuriku–Niigata region. Figure 12 shows estimated vectors of the average winter monsoon winds superimposed on a topographic map of the Toyama Plain, the Tateyama Mountain Range, and the surrounding areas.

According to Yoshizaki and Kato [6], the behavior of a stable cold air mass undergoing forced ascent over mountains is governed by the Froude number ($F_r = u/Nh$). Given that the Tateyama Mountain Range reaches an elevation of 3,000 meters ($h \approx 3,000$ m) and the Siberian cold air mass possesses high static stability ($N \gg 0$), the winter monsoon flow is considered to operate under conditions of a low Froude number ($F_r \ll 1$). In such a state, where potential energy dominates, the inflowing air mass lacks the kinetic energy required to ascend the Tateyama Mountain Range. Consequently, large-scale atmospheric blocking occurs at the mountain foothills facing the Toyama Plain, and the monsoon wind is thought to be diverted horizontally along distinct paths:

1. **Route 1: Coast-Parallel Deflection (Toward Joetsu and Takada)**
   Air masses obstructed by the Tateyama Mountain Range are forced toward the coastline. The airflow then moves into the vicinity of Takada and Nagaoka, where it encounters the Myoko and Echigo mountain ranges and undergoes convergence. This convergence zone acts as a driver for active snowfall in low-lying areas—a phenomenon known as *sato-yuki* (lowland snowfall)—and is believed to account for the high sensitivity to monsoon conditions observed in Takada ($\beta_2 = 22.722$) and Nagaoka ($\beta_2 = 18.116$).

2. **Route 2: Alpine Valley Channeling (Toward Shirakawa)**
   A portion of the airflow obstructed by the Tateyama Mountain Range flows into the narrow valleys of the Sho and Jinzu Rivers. Air masses entering these mountain corridors advance deep into the mountainous interior while undergoing horizontal compression (the nozzle effect), with the resulting impact manifesting at Shirakawa ($\beta_2 = 26.238$). Enclosed by the steep Ryohaku Mountains, this funnel-like zone of airflow convergence traps and lifts concentrated moisture, producing heavy snowfall and resulting in high monsoon sensitivity; conversely, this effect suggests that monsoon sensitivity in Toyama remains relatively low.

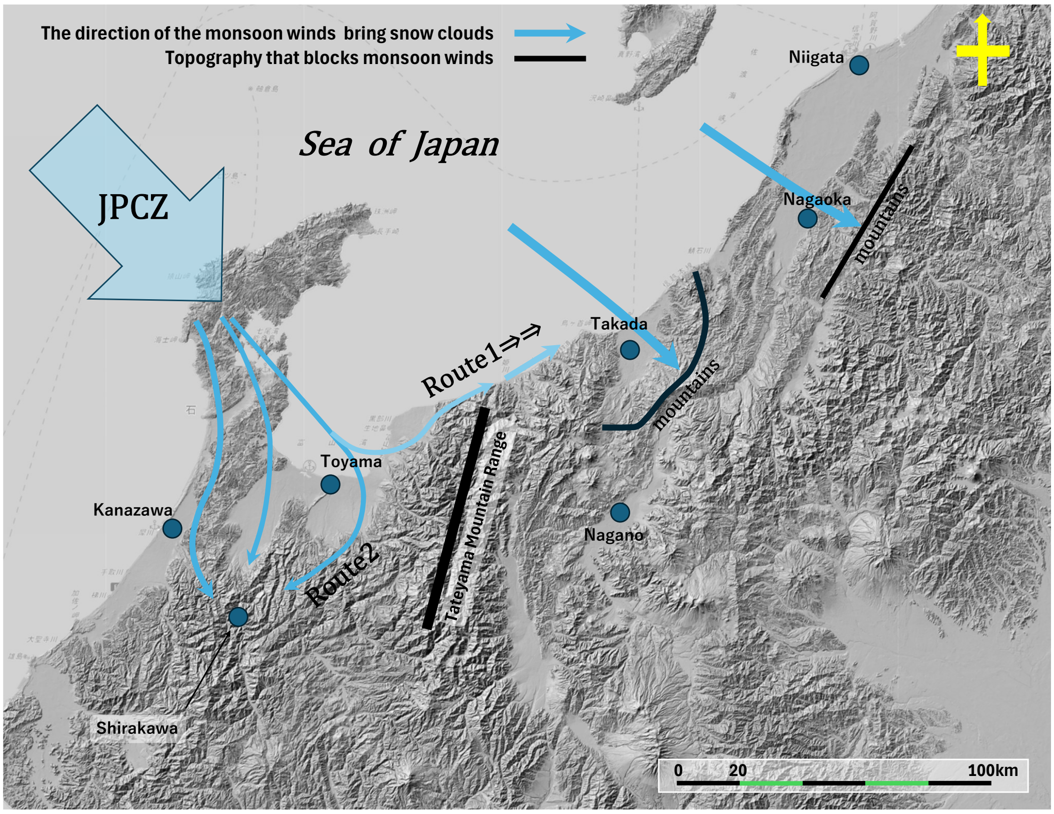

Figure 12: Estimated winter wind-flow vectors overlaid on the topography of the Hokuriku region. This figure illustrates airflow bifurcation paths resulting from the blocking effect of the Tateyama Mountain Range under low Froude number conditions ($F_r \ll 1$): Route 1 (deflection along the coastline toward the Takada and Nagaoka areas) and Route 2 (channeling through valleys toward the Shirakawa area); these paths reflect spatial variations in monsoon sensitivity (β_2).

References

[1] Matsuda, H., & Homma, S. (2026). Data-Driven Extraction of Spatiotemporal Causal Networks of Extreme Snowfall Based on Long-Term Observations in the Japanese Archipelago. *EarthArXiv* (Preprint) https://doi.org//10.31223/X5J48S.

[2] Hanawa, K., et al. (1988). Surface thermal conditions in the western North Pacific during the ENSO events. *Journal of the Meteorological Society of Japan*, 66(3), 445-456.

[3] Matsumura, S., & Xie, S.-P. (1998). Effects of the winter monsoon on interannual climate variability over the Japanese Islands and the Sea of Japan. *Tenki*, 45(10), 781–791 (in Japanese).

[4] National Centers for Environmental Information (NCEI). (2025). *Climate Data Online: Global Summary of the Month (GSOM)*. National Oceanic and Atmospheric Administration. https://www.ncei.noaa.gov/cdo-web/

[5] Yamazaki, A., Honda, M., & Kawase, H. (2019). Regional snowfall distributions in a Japan-Sea side area of Japan associated with jet variability and blocking. *Journal of the Meteorological Society of Japan. Series II*, 97(1), 205-226.https://doi.org//10.2151/jmsj2019-012

[6] Yoshizaki, M., & Kato, T. (2007). *Meteorology of Heavy Rain and Snowfall*. Asakura Publishing.(in Japanese)

[7] Coles, S. G. (2001). *An Introduction to Statistical Modeling of Extreme Values*. Springer-Verlag.

[8] Le Roux, E., Evin, G., Eckert, N., Blanchet, J., & Morin, S. (2022). Non-stationary extreme value analysis of snow loads in the French Alps. *Water Resources Research*, 58(2), e2021WR030190.

[9] Ohori, T., Iida, T., & Kubo, N. (2015). Study on Estimation of GEV Shape Parameter and Practical Aspect of Fixing Parameter's Value. *IDRE Journal*, 295, 1-9.(in Japanese)

[10] Milly, P. C. D., Betancourt, J., Falkenmark, M., Hirsch, R. M., Kundzewicz, Z. W., Lettenmaier, D. P., & Stouffer, R. J. (2008). Stationarity is dead: Whither water management? *Science*, 319(5863), 573–574.

[11] Hayashi, H., Tachikawa, Y., & Shiiba, M. (2015). Non-stationary hydrologic frequency analysis using time dependent parameters and its model selection. *Journal of Japan Society of Civil Engineers, Ser. B1 (Hydraulic Engineering)*, 71(4), I_277-I_282. (in Japanese)

[12] Cheng, L., AghaKouchak, A., Gilleland, E., & Katz, R. W. (2014). Non-stationary extreme value analysis in a changing climate. *Climatic Change*, 127(2), 353-369.

[13] Friedman, J., Hastie, T., & Tibshirani, R. (2008). Sparse inverse covariance estimation with the graphical lasso. *Biostatistics*, 9(3), 432-441.

[14] Kitagawa, G., & Gersch, W. (1984). A smoothness priors–state space modeling of time series with trend and seasonality. *Journal of the American Statistical Association*, 79(386), 378–389.

[15] Shimizu, S., Hoyer, P. O., Hyvärinen, A., & Kerminen, A. (2006). A linear non-Gaussian acyclic model for causal discovery. *Journal of Machine Learning Research*, 7, 2003-2030.

[16] Shimizu, S., Inazumi, T., Sogawa, Y., Hyvärinen, A., Kawahara, Y., Washio, T., Hoyer, P. O., & Bollen, K. (2011). DirectLiNGAM: A Direct Method for Learning a Linear Non-Gaussian Structural Equation Model . *Journal of Machine Learning Research*, 12, 12251248

[17] Dijkstra, E. W. (1959). A note on two problems in connexion with graphs. *Numerische Mathematik*, 1(1), 269-271.

[18] Fredman, M., & Tarjan, R. E. (1987). Fibonacci Heaps and Their Uses in Improved Network Optimization Algorithms. *Journal of the Association for Computing Machinery*, 34(3), 596-615.

[19] Matsuo, T., Sasyo, Y., & Sato, Y. (1981). Relationship between types of precipitation on the ground and surface meteorological elements. *Journal of the Meteorological Society of Japan*, 59(4), 462-476.